





# The dispersive potential-vorticity dynamics of coastal outflows

M. Nguyen<sup>1</sup>  and E.R. Johnson<sup>1</sup> 

<sup>1</sup>Department of Mathematics, University College London, London WC1E 6BT, UK

Corresponding author: M. Nguyen, [zcahmng@ucl.ac.uk](mailto:zcahmng@ucl.ac.uk)

(Received 4 October 2024; revised 16 February 2025; accepted 19 March 2025)

This paper discusses the propagation of coastal currents generated by a river outflow using a 1 1/2-layer, quasigeostrophic model, following Johnson *et al.* (2017) (JSM17). The model incorporates two key physical processes: Kelvin-wave-generated flow and vortical advection along the coast. We extend JSM17 by deriving a fully nonlinear, long-wave, dispersive equation governing the evolution of the coastal current width. Numerical solutions show that, at large times, the flow behaviour divides naturally into three regimes: a steady outflow region, intermediate regions consisting of constant-width steady currents and unsteady propagating fronts leading the current. The widths of the steady currents depend strongly on dispersion when the constant outflow potential-vorticity anomaly is negative. Simulations using contour dynamics show that the dispersive equation captures the full quasigeostrophic behaviour more closely than JSM17 and give accurate bounds on the widths of the steady currents.

**Key words:** hydraulic control, quasi-geostrophic flows, waves in rotating fluids

## 1. Introduction

River outflows and their associated boundary fronts strongly influence the ocean and thermohaline circulation (Rahmstorf 2003), where less dense freshwater flows entering higher-density oceanic waters generate movement across the globe. Freshwater input from rivers introduced by the Arctic Ocean has been found to slow the distribution of heat throughout the Northern Hemisphere (Holliday *et al.* 2020). Moreover, the mixing of ocean and coastal waters generated by outflow currents determines nutrient transport and the subsequent distribution of phytoplankton populations (Ajani *et al.* 2020). Sun *et al.* (2022) specifically emphasise how complex interactions between different river flows



Figure 1. Winter sediment plumes from the Yangtze River spreading into the East China Sea forming a ‘shelf’ of water stretching leftwards (data from the MODIS satellite, 2017), made visible by tidal stirring of bottom sediments (Luo *et al.* 2017).

affect the distribution of the phytoplankton community in coastal waters of South Korea. On a smaller scale, the Hawkesbury River estuary in Australia is a source of nutrient-dense waters transported by the river plume (Li *et al.* 2022), directly influencing the marine taxonomy of the river mouth. Wang *et al.* (2022) further note that coastal and estuarine fronts led by river discharges are responsible for the accumulation of pollutants and microplastics.

Growing evidence relates increasing river discharge to rising coastal sea levels, as currents can be trapped along the coast. With the intensifying hydrological cycle (Pratap & Markonis 2022), Tao *et al.* (2014) predict up to a 60 % increase in discharge from the Mississippi River basin over the next century, the largest source of water drainage from North America into the Atlantic Ocean. Piecuch *et al.* (2018) examine how variable river discharge influences oceanic circulation and how this contributes to rising sea levels on the United States East Coast. Furthermore, from Atlantic and Gulf coast data, they suggest that river discharge is responsible for up to 15 % of the annual sea-level variance.

Numerical studies of river outflows (Mestres *et al.* 2007) examine how changes in river width, inlet transport and the Coriolis parameter affect the surface plume width given a constant outflow discharge. Tides, wind forcing and unsteady outflows can also influence the evolution of the coastal front (Southwick *et al.* 2017). In the Northern Hemisphere freshwater from rivers could be expected to turn right (in the direction of the Coriolis force). There are, however, clear indications of leftward propagation, such as the suspended sediments that form the Yangtze River plume front (figure 1). Johnson *et al.* (2017, JSM17 herein) capture both phenomena by using a theoretical long-wave approximation to the 11/2-layer, quasigeostrophic (QG) equations where fluid expelled from a single-channel outflow is driven along the coast by a Kelvin wave (KW) and vortical advection. They use an idealised model where the current and upper layer have piecewise constant vorticity following the model by Pratt & Stern (1986). This most closely applies to large-scale fronts that are governed by near-geostrophic dynamics (Nagai *et al.* 2006) but remains

useful in describing buoyant discharges by capturing much of the essential physics of gravity-current outflows where less dense fluid enters denser fluid, including for surface-advected buoyant estuarine outflows in the Hudson river (Chant *et al.* 2008). Kubokawa (1991) gives contour dynamics (CD) simulations that closely match the outflow gyre modes in the Tsugaru Strait. McCreary *et al.* (1997) add entrainment and horizontally varying salinity, obtaining a 11/2-layer ageostrophic model that contains the simplified model of Kubokawa (1991) in the small Rossby number limit. Horner-Devine *et al.* (2006) and Thomas & Linden (2007) model river plumes in the laboratory as coastal currents in geostrophic balance and note features like the upstream expanding bulge captured in the theory of JSM17 and Johnson (2023). Gregorio *et al.* (2011) repeat the experiments from Thomas & Linden (2007), obtaining good agreement with numerical coastal outflow simulations (regional ocean modelling system, or ROMS) when horizontal viscous forces are small. These models consider buoyant outflows that are not in contact with the ocean floor and thus do not address the dynamics of outflows of fluid denser than the ambient which are strongly affected by bottom drag. The QG models also exclude internal waves involved in turbulent mixing when the outflow meets the ambient. If the fluid density differences are large then turbulent stresses can become important, particularly in sub-mesoscale fronts, although Pham & Sarkar (2019) still observe cold freshwater-carrying surface gravity currents, including those far from the coast, in the Bay of Bengal reminiscent of the laboratory experiments by Thomas & Linden (2007). Mendes *et al.* (2021) note that such turbulence is unlikely to be important in the Duoro river plume where fluid density differences are small. More sophisticated two-layer outflow models describing the discharge of the Ganges-Brahmaputra-Meghna mega-delta (Kida & Yamazaki 2020), a major freshwater source in the Bay of Bengal, also show how fronts from the individual river branches that form the delta play an important role in the dynamics of the geostrophically balanced freshwater river plume.

Jamshidi & Johnson (2019, JJ19 herein) extend JSM17 to order-unity Rossby numbers using the semigeostrophic equations to investigate the validity of the QG approximation. The extension admits a KW propagating along the coast at a finite speed contrasting with the QG limit where the KW propagates infinitely fast. Even at Rossby numbers of order unity, the outflow behaviour remains qualitatively similar: the KW simply sets the boundary condition for the more slowly moving vortical fluid, as noted in § 2. We thus continue with the simpler QG model of JSM17, but capture more detail in the solutions by studying the dispersive potential-vorticity (PV) equation which adds higher-order terms to the leading-order hydraulic PV equation. The dispersive equation captures the dynamics of the frontal waves that appear on the edge of the outflow current in the full CD integrations, but are necessarily absent in the hydraulic theory of JSM17, and also the compound-wave structures (described in § 4.2) seen in the CD integrations there. The dispersive equation predicts new behaviour such as the formation of dispersive-shock waves (DSWs) and wall-bounded wavetrains, not seen in the limited number of CD integrations in JSM17 but found in the CD integrations here, indicating a dynamical regime where coastal outflows might break into eddy trains. Perhaps the most important result is the demonstration that, in certain parameter regimes, the width of the coastal current cannot be determined uniquely from global quantities like the volume flux, PV and density contrast: the width also depends on the details on the geometry of the outflow, which appears below simply as the width of the outflow relative to the current width. Although a local theory can predict the balance in the current, the width of the current varies with the width of the outflow even when the global quantities are unchanged. The analysis builds on the methods in Jamshidi & Johnson (2020, JJ20 herein) who derive the dispersive equation for a coastal

current of constant flux along a wall and analyse the Riemann problem for the adjustment of a step change in the width of an alongshore current using El's dispersive-shock fitting technique (El 2005).

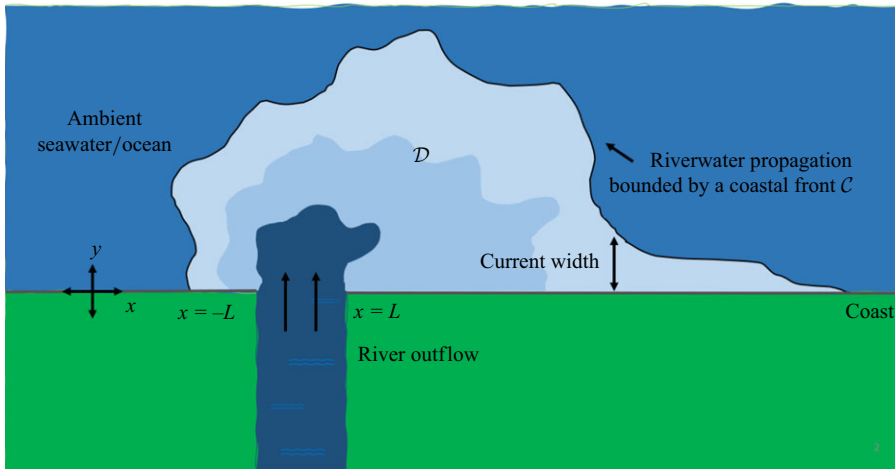
Section 2 describes the idealised flow geometry considered here, governed by the 11/2-QG equations, and presents the leading-order hydraulic limit of the equations and their first-order dispersive correction. Away from the source, the system supports travelling waves of fixed form and the equations governing these are noted in § 2.3. The flow evolves to divide naturally at large times into three regimes: a steady region containing the outflow, constant-width currents leading away from the outflow regions and unsteady propagating frontal regions leading the constant-width currents. Section 3 considers the outflow region, presenting numerical solutions for the asymptotically steady flow there and discussing the transition between subcritical and supercritical flow across the outflow. The widths of the outflow currents for negative PV outflows are shown to depend strongly on the strength of the dispersion. Section 4 describes the various compound-wave structures observed in the fronts leading the constant-width currents, and § 5 compares predictions from the dispersive long-wave theory with integrations of the full QG equations. The results are summarised briefly in § 6.

## 2. Formulation

We consider a river outflow model where fluid is released from a constant depth inlet and flows along the coast into a half-space consisting of an upper active layer, comprising the expelled fluid and displaced ambient ocean water, and an ambient lower layer of infinite depth. The flow geometry is shown from a plan view in figure 2(a) and a side view in figures 2(b)(i), 2(b)(ii). We take Cartesian coordinates  $\mathcal{O}xyz$ , with  $x$  along the coast,  $y$  offshore and  $z$  vertical. The system rotates with Coriolis parameter  $f$  about the  $z$ -axis. Here,  $D_s$  denotes the depth of the inlet,  $D$  the depth of the upper ambient fluid and  $L$  the half-width of the outflow lying along a vertical coast  $y = 0$ . We denote the connected region of the expelled fluid by  $\mathcal{D}$ , bounded by the contour  $\mathcal{C}$  which separates expelled fluid from the ambient. At times  $t > 0$ , fluid is released from the outflow into the half-space  $y > 0$  with a constant discharge rate that is independent of the width of the source and constant non-zero PV denoted by  $\Pi^*$ . The expelled and ambient fluid in the upper layer has density  $\rho_1$  while the lower layer has zero PV and density  $\rho_2 > \rho_1$ , with  $|\rho_1 - \rho_2| \ll \rho_2$  so the Boussinesq approximation is valid. This layered system satisfies the 11/2-layer QG equations provided the relative depth change between the inlet and the active layer is small, i.e.  $|D - D_s| \ll D$ . Typical velocities are small compared with the speed of long free-surface water waves, so the surface  $z = 0$  can be taken as effectively rigid with the dynamics restricted to the interface between the layers. The difference between the potential vorticity of the expelled fluid and the upper ambient fluid, defined as the PV anomaly (PVa),  $\Pi_0 := \Delta\Pi^* = f/D_s - f/D$ , is positive if the outflow depth is deeper than the inlet depth  $D_s < D$ , or negative if  $D_s > D$ . Herein (as in JJ20) we denote PVa as just PV for brevity.

The evolution of the vortical boundary  $\mathcal{C}$  is governed by the equation for the conservation of QG PV and since the PV has constant magnitude the evolution is entirely determined by the instantaneous position of  $\mathcal{C}$ . This allows the full, unapproximated evolution to be computed accurately using contour dynamics (§ 5, Dritschel 1988). To derive a long-wave equation we restrict attention to flows where the coastal front  $\mathcal{C}$  does not overturn and the current width can be written as  $y = Y(x, t)$ . This is true for gently propagating coastal fronts but the CD integrations § 5 suggest that overturning can occur, particularly for flows begun impulsively, and is discussed separately. The QG equations

(a) Plan view



(b) Side view

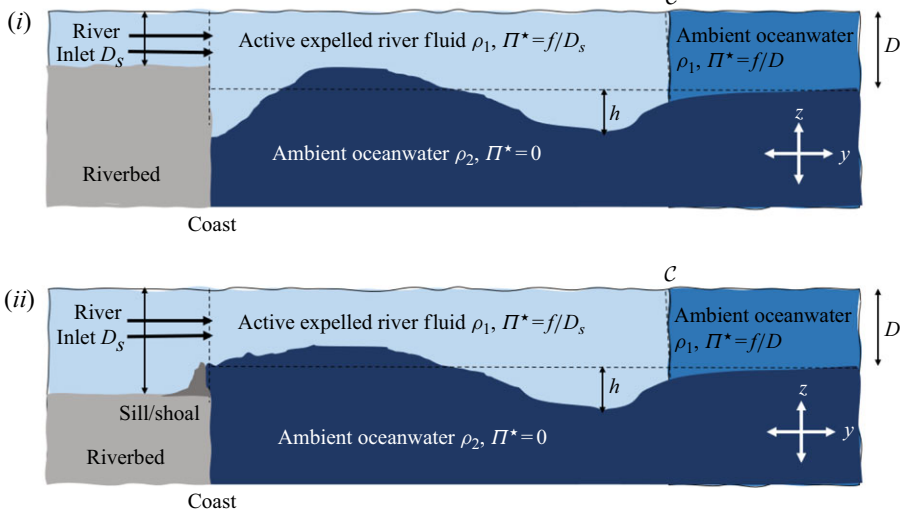


Figure 2. A schematic of a river outflow expelling fluid at  $t > 0$  from an inlet with depth  $D_s$  into the upper layer of depth  $D$ . The lower layer of ambient ocean water below has infinite depth hence  $\Pi^* = 0$ . The subsequent displacement of the interface between the layers is denoted by  $h$ . (a) The plan view of a river source of half-width  $L$  where the expelled fluid evolves to form a region  $\mathcal{D}$  enclosed by a closed coastal front  $\mathcal{C}$  (including the coast boundary  $y = 0$ ). (b) The side view where (b)(i): the outflow depth is deeper than the river inlet, so there is positive PVa generation. (b)(ii): outflow depth is shallower than the inlet (due to the presence of a shoal say) so there is negative PVa generation.

allow the introduction of a streamfunction

$$\psi(x, y, t) = \frac{g'h(x, y, t)}{fQ_0}, \quad (2.1)$$

where  $h(x, y, t)$  is the interface displacement. Here,  $Q_0$  is the area flux expelled by the outflow (with total volume  $Q_0D$ ),  $g'$  is the reduced gravity, with the horizontal velocities of the flow given by  $(u, v) = (-\psi_y, \psi_x)$ . Spatial and temporal scales are non-dimensionalised (with choices justified, along with other quantities below, in JSM17)



according to the vortex length  $L_v$  and advection time scale  $T_v$  where

$$L_v = (Q_0/|\Pi_0 D|)^{1/2}, \quad T_v = L_v^2/Q_0. \quad (2.2)$$

We define  $W$  to be the non-dimensionalised half-width (herein just width) of the outflow such that  $W = L/L_v$ . The non-dimensional governing equation becomes

$$q = \nabla^2 \psi - \frac{1}{a^2} \psi = \begin{cases} 0 & y > Y(x, t) \\ \Pi & 0 < y < Y(x, t), \end{cases} \quad (2.3)$$

where  $\nabla^2 = \partial/\partial x^2 + \partial/\partial y^2$  is the Laplacian operator, the constant PV is non-dimensionalised as  $\Pi = \Pi_0/|\Pi_0|$  so that  $\Pi$  gives the sign of the expelled PV and  $a = L_R/L_v$  is the ratio of the Rossby radius of deformation for the interface  $L_R = \sqrt{g'H}/f$  to the vortical length scale  $L_v$ . The parameter  $a$  is later referred to as simply the Rossby radius. It measures the ratio of the strength of advection by the image vorticity to that by the KW induced flow. The jump in vorticity across  $y = Y(x, t)$ , i.e. the material line  $\mathcal{C}$ , supports a frontal Rossby wave that propagates unidirectionally with high PV to its right and so in the same direction as the flow induced by the image, in the coastal wall, of the vortical current. Thus for  $\Pi = +1$ , the frontal Rossby wave and advection by image vorticity combine with the KW to reinforce the rightward turning flow. For  $\Pi = -1$ , the frontal Rossby wave and the image vorticity advection oppose the KW.

We denote the flux function of the source outflow by  $Q(x)$  with width  $W$  along the coast  $y = 0$ . The fluid is impulsively expelled at  $t > 0$  given by the no-flux boundary condition (2.4), and far from the coast the fluid is stationary so

$$\psi(x, 0, t) = Q(x), \quad (2.4)$$

$$\psi \rightarrow 0, \quad y \rightarrow \infty. \quad (2.5)$$

Here,  $Q(x \leq -W) = 0$ ,  $Q(x \geq W) = 1$  (so the area flux expelled is 1 normalised from  $Q_0$ ). JSM17 and JJ20 show that the asymmetry in  $Q(x)$  arises necessarily from the KW generated when the source is switched on. The KW propagates to the right at finite speed in JJ20 and instantaneously in JSM17 to set the coastal boundary condition.

The remaining condition is the kinematic boundary condition that fluid particles on the coastal front remain on the coastal front  $\mathcal{C}$

$$Y_t = [\psi(x, Y(x, t))]_x. \quad (2.6)$$

### 2.1. The leading-order hydraulic solution

Rescaling (2.3) using the long-wave variables

$$X = \varepsilon x, \quad T = \varepsilon t, \quad (2.7)$$

where  $\varepsilon = 1/W$ , and expanding  $\psi$  in terms of  $\varepsilon$  gives

$$\psi(X, y, T) = \psi^0 + \varepsilon^2 \psi^1 + \mathcal{O}(\varepsilon^4). \quad (2.8)$$

We substitute (2.8) into (2.3) which is matched with the leading-order  $\varepsilon^0$  and first-order  $\varepsilon^2$  terms. This derivation is summarised from JJ20, with the modification that  $Q(x)$  here varies instead of being constant in  $x$ . Directly evaluating  $\psi^0$  at the coastal front  $y = Y(X, T)$  gives

$$\psi^0(X, Y, T) = Q_e(X, Y, T) = -\frac{a^2 \Pi}{2} + (Q(X) + a^2 \Pi)e^{-Y/a} - \frac{\Pi a^2}{2}e^{-2Y/a}. \quad (2.9)$$

The parameter  $Q_e(X, Y, T)$  gives the net rightward flux of the oceanic fluid at  $X$  with  $Q(X) - Q_e(X, T)$  giving the net rightward flux in the coastal current. The kinematic boundary condition (2.6) at the leading order becomes, in terms of  $x$  and  $t$ ,

$$Y_t + \left[ \left( \frac{Q(x)}{a} + a\Pi \right) e^{-Y/a} - a\Pi e^{-2Y/a} \right] Y_x + Q'(x) e^{-Y/a} = 0. \quad (2.10)$$

Equation (2.10) is a first-order nonlinear partial differential equation (PDE) with disturbance propagation speed  $C(Y)$  given by

$$C(Y) = \left( \frac{Q(x)}{a} + a\Pi \right) e^{-Y/a} - a\Pi e^{-2Y/a}, \quad (2.11)$$

governing the leading-order behaviour of the coastal front  $Y(x, t)$ . At each  $x$  the disturbance speed  $C(Y)$  is the sum of the frontal Rossby-wave speed and the fluid speed at the front. Information travels to the right when  $C(Y) > 0$  and to the left when  $C(Y) < 0$ . This behaviour is directly analogous to the hydraulic behaviour in free-surface channel flow and has been described as Rossby-wave hydraulics (see, for example, Johnson & Clarke 2001). Since the frontal Rossby wave is the sole wave present, solutions of (2.10) will be described simply as hydraulic solutions.

## 2.2. The dispersive correction

The next order in  $\varepsilon$  gives the  $\mathcal{O}(\varepsilon^2)$  correction to  $\psi$  on  $y = Y(X, T)$  as

$$\begin{aligned} \psi^1(X, Y, T) = & -\frac{a^3\Pi}{4} Y_{XX} + \left( \frac{a^2}{2} \Pi Y Y_{XX} + \frac{a^3}{4} \Pi Y_{XX} - \frac{a\Pi}{2} Y (Y_X)^2 \right) e^{-2Y/a} \\ & + \frac{a}{2} Q_{XX}(X) Y e^{-Y/a}. \end{aligned} \quad (2.12)$$

The dispersive kinematic boundary condition (2.6) including these dispersive terms becomes

$$\begin{aligned} Y_t + \left[ \frac{a^2\Pi}{2} e^{-2Y/a} - \left( Q(x) + a^2\Pi \right) e^{-Y/a} \right]_x + \frac{a^3\Pi}{4} Y_{xxx} \\ - \Pi \left[ \left( \frac{a^2}{2} Y Y_{xx} - \frac{a}{2} Y (Y_x)^2 + \frac{a^3}{4} Y_{xx} \right) e^{-2Y/a} \right]_x - \left[ \frac{a}{2} Q_{xx}(x) Y e^{-Y/a} \right]_x = 0. \end{aligned} \quad (2.13)$$

Expanding (2.13) gives the alternative form of the dispersive kinematic boundary condition

$$\begin{aligned} Y_t + \left[ \left( \frac{Q(x)}{a} + a\Pi \right) e^{-Y/a} - a\Pi e^{-2Y/a} \right] Y_x \\ + \frac{a^3\Pi}{4} Y_{xxx} - \Pi \left( (Y - a/2)(Y_x)^3 + \frac{a^3}{4} Y_{xxx} + \frac{a^2}{2} Y Y_{xx} - 2aY Y_x Y_{xx} \right) e^{-2Y/a} \\ - Q_x(x) e^{-Y/a} - \frac{a}{2} Q_{xx}(x) Y e^{-Y/a} - \frac{a}{2} Q_{xx}(x) (1 - Y/a) Y_x e^{-Y/a} = 0. \end{aligned} \quad (2.14)$$

While the parameter  $\varepsilon$  no longer appears, the variables  $x, t$  vary slowly. Formally, this means  $1/\varepsilon \equiv W \gg 1$  and  $a$  is of order unity. When  $Q(x)$  narrows to a point source outflow  $W \rightarrow 0$ , its derivatives become large  $Q_x(x) \sim 1/W \gg 1$ , which violates this requirement. The system can, however, still be treated with surprisingly good accuracy (§ 3.2).

### 2.3. The travelling-wave solutions of the dispersive equation

In the regions  $|x| > W$ , where the flux function is constant,  $Q(x) \equiv Q$ , the system supports waves of permanent form (see JJ20 for the case  $Q = 1$ ). We change to moving coordinates by setting  $\xi = x - st$  and look for solutions steady in this moving frame. The governing PV equation (2.14) can then be written in potential form

$$(Y_\xi)^2 = \frac{2}{a^2} \frac{a^3 e^{-2Y/a} - 4a(Q\Pi + a^2)e^{-Y/a} + 2s\Pi Y^2 + \alpha Y + E}{a - (a + 2Y)e^{-2Y/a}} \equiv \frac{2}{a^2} \frac{v(Y, s, \alpha, E)}{\mathcal{G}(Y)}, \quad (2.15)$$

where  $\alpha, E$  are the constants of integration, and  $s$  is the speed of the travelling wave.

JJ20 show that a solitary wave propagating along a background  $Y = Y_\infty$ , with maximum displacement  $Y_1$ , satisfies

$$v(Y = Y_1) = v(Y = Y_\infty) = v'(Y = Y_\infty) = 0, \quad (2.16)$$

where  $'$  denotes differentiation with respect to  $Y$  and a kink soliton joining two different far-field states  $Y_1$  and  $Y_2$  satisfies

$$v(Y = Y_1) = v(Y = Y_2) = v'(Y = Y_1) = v'(Y = Y_2) = 0. \quad (2.17)$$

For given external parameters  $a, Q, \Pi$ , the kink soliton solution also determines a unique coastal intrusion where a current of constant width  $Y_1 = Y_I$  terminates at the coast so  $Y_2 = 0$ . Equation (2.17) determines the constants  $\alpha, E$ , giving the unique intrusion speed  $s_I$  and width  $Y_I$ ,

$$(-a^2 Y_I + 3a^3 + 4aQ\Pi - 2Q\Pi Y_I)e^{2Y_I/a} - (2a^2 Y_I + 4a^3 + 4aQ\Pi + 2Q\Pi Y_I)e^{Y_I/a} + (a^2 Y_I + a^3) = 0, \quad (2.18)$$

$$s_I = \frac{-2a^2 e^{-2Y_I/a} + 4(a^2 + Q\Pi)e^{-Y_I/a} - 2a^2 - 4Q\Pi}{-4Y_I\Pi}. \quad (2.19)$$

Since  $\mathcal{G}, \mathcal{G}' \rightarrow 0$  as  $Y \rightarrow 0$ , and  $v, v' \rightarrow 0$  by construction, the PV front meets the coast with finite gradient

$$(Y_\xi)^2|_{Y=0} = \frac{2\Pi(as_I - Q)}{a^2}. \quad (2.20)$$

Intrusion solutions are shown below to play a significant role in determining the long time behaviour of solutions in certain parameter regimes. A closely related wave type, not present in JJ20, that appears in the outflow problem is a wall-bounded wavetrain. These waves are discussed in detail in § 4.5 and satisfy conditions given by (4.15).

### 3. The outflow region

As in the hydraulic solutions of JSM17, the outflow region controls the development of the solutions both upstream and downstream and so is considered here first. We consider initially the case  $\Pi = -1$ , addressing the case  $\Pi = +1$  in § 3.1.2. For steady flow, (2.6) integrates directly to give

$$F(Y, Y_x, Y_{xx}) := \psi^0(x, Y) + \psi^1(x, Y, Y_x, Y_{xx}) = \Phi, \quad (3.1)$$

for some constant  $\Phi$ , to be determined. As  $x \rightarrow \pm\infty$ , the PV front settles to constant-width currents of upstream width  $Y_-$  and downstream width  $Y_+$  (say). The dispersive term is absent for constant-width currents and so both  $Y_-$  and  $Y_+$  satisfy the hydraulic



form of (3.1) which becomes, from (2.9),

$$\Phi = Q_e(Q=0, Y_-) = Q_e(Q=1, Y_+). \quad (3.2)$$

There are no stationary ( $s=0$ ) non-trivial solutions of (2.15) with  $Q=0$  and so the constant-width solution  $Y=Y_-$  extends to the downstream edge of the source region at  $x=-W$ . In  $x>W$ , where  $Q=1$ , non-trivial stationary solitary waves solutions of (2.15) exist and the solution across the source region must match to part of one of these riding on the background  $Y=Y_+$ . The problem for the flow in the source region can thus be posed as the boundary value problem (BVP)

$$Y=Y_-; \quad x \leq -W, \quad (3.3)$$

$$\psi^0(x, Y) + \psi^1(x, Y, Y_x, Y_{xx}) = \Phi; \quad |x| \leq W \quad (3.4)$$

$$(Y_x)^2 = \frac{2}{a^2} \frac{v(Y, \alpha_+, E_+)}{\mathcal{G}(Y)}; \quad x \geq W, \quad (3.5)$$

with  $Y$  and  $Y_x$  continuous across  $x=\pm W$ .

The constants  $\alpha_+$ ,  $E_+$  are determined using the conditions for the existence of a soliton with  $\Pi=-1$ , lying on  $Y=Y_+$ , in (2.16), and solving (3.4) in the outflow region  $|x| \leq W$  gives the value of  $Y(W) \equiv Y_+$  and  $\Phi$ , allowing (3.5) to be solved from  $x=W$ . Knowledge of  $\Phi$  uniquely determines the widths of the far-field  $Y_+$ ,  $Y_-$  and, by extension, the entire steady system.

We solve this system by truncating the domain at some  $x=\pm L$  for large  $L$  and using a BVP solver (bvp4c/bvp5c) in MATLAB. Equation (3.4) is solved across the entire domain, setting the flux function to be  $Q(x) := Q_4(x)$  in (4.1), which is equivalent to solving (3.3), (3.4), (3.5) separately in each domain and unifying the solutions. Although a shooting method can be used to find  $\Phi$  similarly to Jamshidi & Johnson (2021), the bvp4c/bvp5c solvers handle this automatically on introducing the auxiliary equation

$$\Phi = Q_e(x=-W) = \frac{-a^2 \Pi}{2} + (Q + a^2 \Pi) e^{-Y_-/a} - \frac{\Pi a^2}{2} e^{-2Y_-/a}, \quad (3.6)$$

to be satisfied alongside the ordinary differential equation (ODE). Figure 3 shows the frontal position and streamlines for a typical solution. The entire outflow leaves the source and turns upstream, travelling to an unsteady upstream frontal region in the full problem where some of the fluid turns to form a downstream return current along the PV front. This leaves a central recirculating region just downstream of the outflow, as observed in the experiments of Thomas & Linden (2007) and the ageostrophic integrations of Gregorio *et al.* (2011) and modelled in Johnson (2023). The Rossby frontal wave travels upstream with high PV to its right. Its speed precisely equals the coastal current speed at the dispersive control point, marked as a blue dot on the front, where  $C(Y)=0$ . Upstream of this point  $C(y)<0$  and the flow is subcritical, with information propagating upstream. Downstream of this point  $C(y)>0$  and the flow is supercritical, with information propagating downstream. This identification of hydraulic regimes is justified in the following section.

### 3.1. Hydraulic control

Consider wavelike perturbations of a steady solution  $Y=Y_s(x)$  of (2.14) of the form

$$Y(x, t) = Y_s(x) + \hat{e} y(x, t), \quad \hat{y} \sim \mathcal{O}(1), \quad (3.7)$$

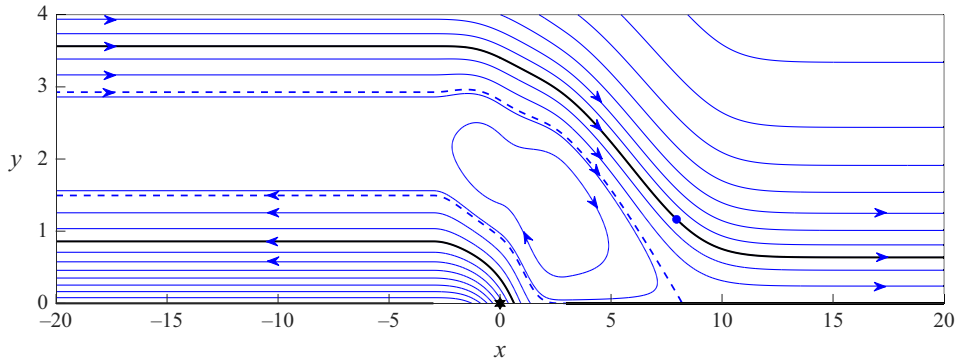


Figure 3. The streamlines (blue) and of a steady dispersive solution with  $a = 1.3$ ,  $\Pi = -1$ , and source lying within  $|x| \leq W = 3$ . The streamline coinciding with the coastal front  $Y(x)$  is marked in black. The dispersive control point where  $C(Y)$  vanishes is shown by a blue circle. The blue-dashed streamline  $\psi = 1$  bounds a region of recirculating flow.

where  $\hat{\varepsilon} \ll 1$ . Then, to order  $\hat{\varepsilon}$ , (2.14) becomes

$$\frac{\partial \hat{y}}{\partial t} + \hat{C} \frac{\partial \hat{y}}{\partial x} = f(\hat{y}, \hat{y}_{xx}, \hat{y}_{xxx}), \quad (3.8)$$

$$\hat{C} = C(Y_s) + C^1, \quad (3.9)$$

$$C^1 = -\Pi \left( 3 \left( Y_s - \frac{a}{2} \right) (Y_s')^2 - 2aY_s Y_s'' \right) e^{-2Y_s/a} - \frac{a}{2} Q''(x) (1 - Y_s/a) e^{-Y_s/a}. \quad (3.10)$$

Both the forcing function  $f$  and the wavespeed perturbation  $C^1$  are of order  $\varepsilon^2$  and so (3.8) can be regarded, at leading order in the long-wave parameter  $\varepsilon$ , as a first-order PDE with disturbance propagation speed  $\hat{C} = C(Y) + \mathcal{O}(\varepsilon^2)$ . As in the hydraulic limit,  $C(Y)$ , given by (2.11), is the local speed of infinitesimal perturbations to the steady dispersive equation.

### 3.1.1. The $\Pi = -1$ case

The unsteady hydraulic solution (2.10) in JSM17 evolves to be critically controlled at the downstream edge  $x_c = W$  of the source and thus sets  $Y_+$  and  $Y_-$ . In this case, (3.1) becomes

$$Q_e(Y = Y_-, Q = 0, \Pi) = Q_e(Y = Y_+, Q = 1, \Pi) = \Phi, \quad (3.11)$$

where  $Q_e \equiv \psi^0$  is the leading-order (hydraulic) streamfunction evaluated at the PV front. Requiring flow to be critically controlled gives some essential conditions in the hydraulic equation. From JSM17,  $Y_+$  is determined by setting the width at the downstream edge control point  $C(Y_+) = 0$  and  $Y_-$  can be derived using equation (3.11), giving

$$Y_+ := (Y_+)_{hyd, -1} = a \ln \left( \frac{a^2}{a^2 - 1} \right), \quad Y_- := (Y_-)_{hyd, -1} = a \ln \left( \frac{a^4 + a^2 \sqrt{2a^2 - 1}}{(a^2 - 1)^2} \right). \quad (3.12)$$

When  $a \leq 1$ , these expressions fail and steady solutions no longer exist.

As shown above, the control point for dispersive solutions also occurs when  $C(Y) = 0$ , however, as the dispersive solution differs from the hydraulic solution, the control point, although occurring at the same value of  $Y$ , lies at a different value of  $x_c \neq W$ , which can only be determined once the dispersive solution is known. Since the control point is fixed

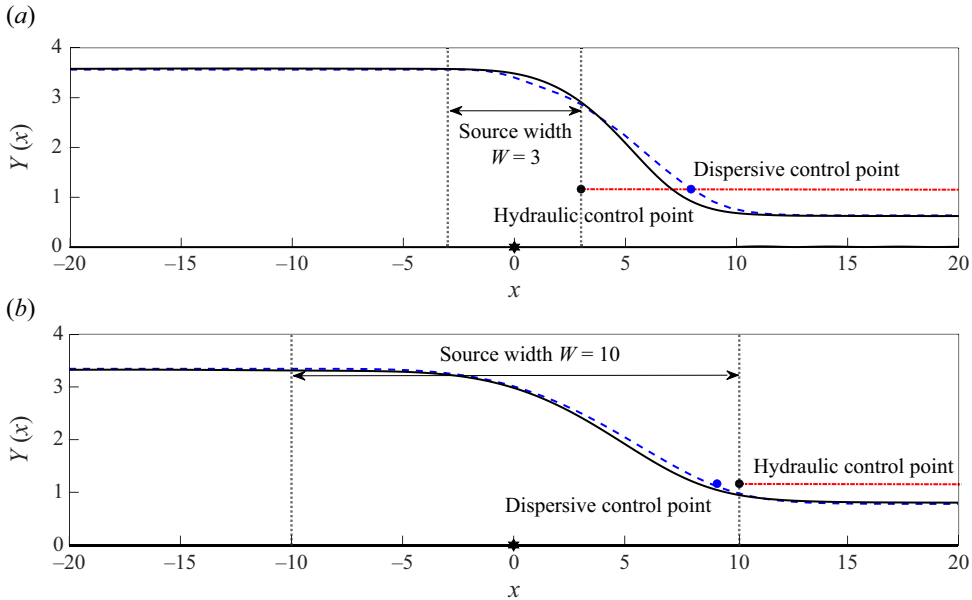


Figure 4. The steady dispersive solutions (shown in blue) for  $a = 1.3$ ,  $\Pi = -1$  plotted for source widths: (a)  $W = 3$ , (b)  $W = 10$  with the outflow centred at  $x = 0$  (marked as a filled star). For comparison, the full QG solutions (in black) is shown for  $t = 500$ . The locations of the hydraulic and dispersive control points are shown by a black and blue filled circle, respectively. The red line denotes the hydraulic rarefaction at  $t = 10\,000$ , an almost constant-width current extending from the hydraulic control point.

at  $x_c = W$  in the hydraulic solutions the current widths  $Y_-$ ,  $Y_+$  do not change with the outflow width. The current width in the dispersive solutions varies with the width of the outflow and so does the position of the control point.

Figure 4 compares the numerical steady dispersive solution with the full QG solution (using the contour dynamics method of § 5) run until  $Y_-$  and  $Y_+$  converge to their steady values. The widths  $Y_{\pm}$  are well predicted for source widths  $W = 3, 10$ , significantly improving on the large-time limit of the downstream hydraulic rarefaction solution shown in red. The  $Y$  displacements of the hydraulic (black) and dispersive (blue) control points are the same, but the values of  $x_c$  differ. The control point for  $W = 10$  lies closer to the downstream outflow than that for  $W = 3$  since the solution converges to the hydraulic solution as  $W$  increases.

### 3.1.2. The $\Pi = +1$ case

Critical control in the hydraulic solution for  $\Pi = +1$  occurs at the upstream edge of the source outflow at  $x_c = -W$  giving a steady solution with no current upstream. For  $x > -W$ ,  $C(Y) > 0$ , so the flow is supercritical everywhere. As shown in JSM17, this gives remarkably accurate results compared with the full problem, predicting the upstream and downstream steady current widths as

$$(Y_-)_{\text{hyd}, +1} \equiv 0, \quad (Y_+)_{\text{hyd}, +1} = a \ln \left( 1/a^2 + 1 + \sqrt{1/a^4 + 2/a^2} \right). \quad (3.13)$$

The dispersive equation also establishes a control point, but this causes the front to cross the coast, reaching negative  $Y$  values. This invalidates the solutions and so comparison with the full problem is omitted. The dispersive PV equation improves on hydraulic solutions only for negative PV.

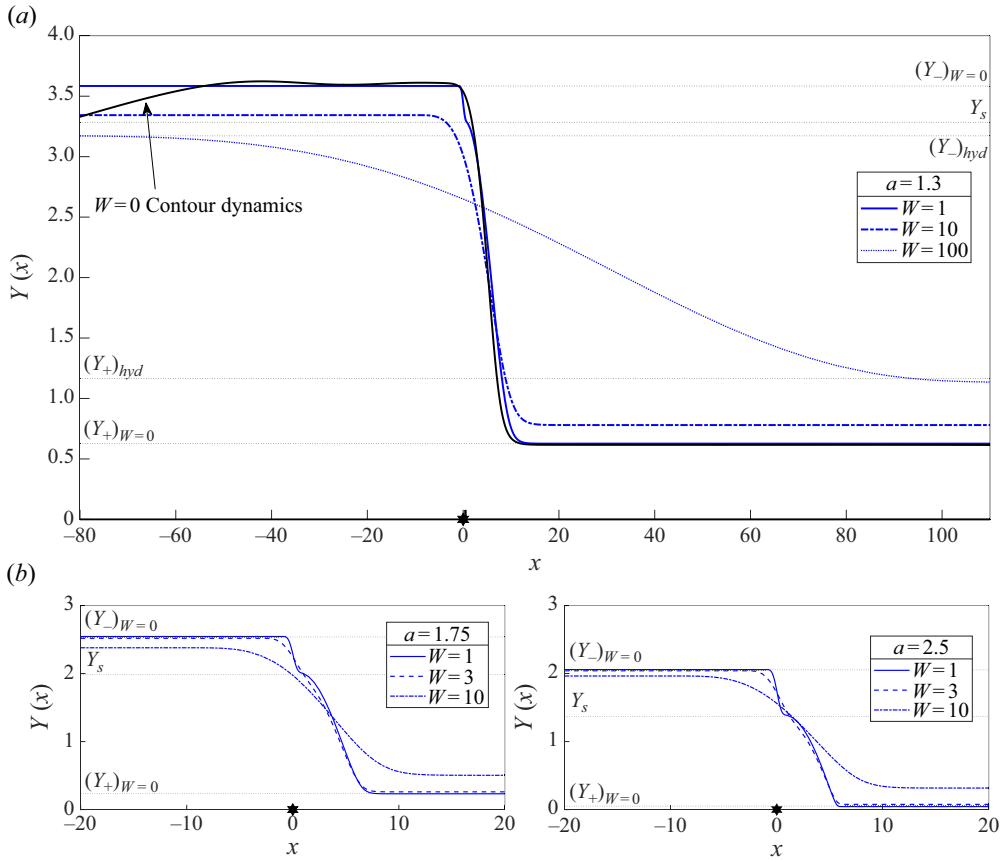


Figure 5. (a) The steady dispersive solutions (blue) at  $a = 1.3$ ,  $\Pi = -1$  shown for different widths  $W = 1, 10, 100$ , compared directly with the contour dynamics for  $W = 0$  at  $t = 1000$  (shown in black). Also overlaid is the comparison (dotted lines) with the hydraulic and dispersive predictions of the current widths  $(Y_{\pm})_{hyd}$ ,  $(Y_{\pm})_{W=0}$ . (b) As above but for  $a = 1.75$  and  $a = 2.5$  ( $W = 1, 3, 10$ ).

### 3.2. The narrow source limit, $W \rightarrow 0$

The governing PV equation (2.14) is not formally valid for narrow outflows with  $W \lesssim \mathcal{O}(1)$ . However, over long times, the dispersive equation for  $\Pi = -1$  captures the far-field values  $(Y_-, Y_+)$  of the full problem well in this regime (figure 5). It is therefore useful to analyse the dispersive equation in this limit and extend the analysis of (2.14) to all  $W$ .

In the steady solutions for  $\Pi = -1$  the far-field currents join through a (truncated) soliton which connects the downstream constant-width current  $Y_+$  to an intermediate point  $Y = Y_s$  at  $x = W$  that is subsequently linked smoothly across the outflow region  $|x| < W$  to the constant-width current  $Y(x = -W) = Y_-$ . As shown in figure 5, for decreasing source widths the solution the cross-outflow matching becomes progressively steeper, approaching a vertical jump at  $x = 0$  as  $W \rightarrow 0$ . The soliton truncates at its maximum height to minimise the width of the jump. Figure 6 shows this suggested shape of the coastal front for a point source outflow. Thus we require that as  $W \rightarrow 0$ ,  $Y(x)$  satisfies

$$Y(x \rightarrow 0^-) = Y_-, \quad Y(x \rightarrow 0^+) = Y_s, \quad Y_x(x \rightarrow 0^-) = 0, \quad Y_x(x \rightarrow 0^+) = 0, \quad (3.14)$$

with  $Y_s$  giving the width from the coast of the soliton.

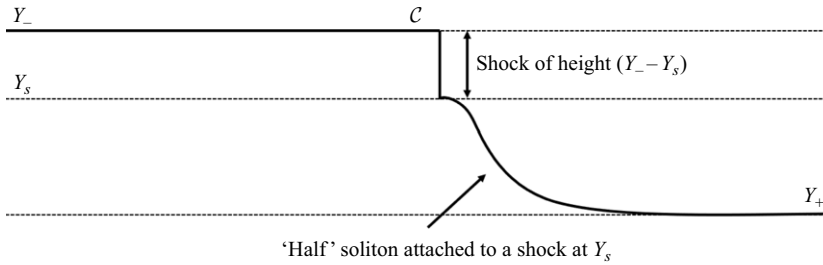


Figure 6. The suggested structure of the coastal front  $C$  for  $\Pi = -1$  as the outflow width  $W \rightarrow 0$  in dispersive flow. A shock links the constant-width current in  $x < 0$  to a soliton asymptoting to  $Y_+$ .

Integrating the steady form of (2.13) once gives

$$\begin{aligned} \frac{a^3 \Pi}{4} Y_{xx} - \Pi \left[ \left( \frac{a^2}{2} Y Y_{xx} - \frac{a}{2} Y (Y_x)^2 + \frac{a^3}{4} Y_{xx} \right) e^{-2Y/a} \right] - \frac{a}{2} Q''(x) Y e^{-Y/a} \\ + \frac{a^2 \Pi}{2} e^{-2Y/a} - \left( Q(x) + a^2 \Pi \right) e^{-Y/a} - \Phi = 0, \end{aligned} \quad (3.15)$$

with constant of integration  $\Phi = Q_e(Y_-)$ . On integrating (3.15) across the outflow from  $-W$  to  $W$  with respect to  $x$ , and taking the limit  $W \rightarrow 0$ , the integral involving the last line of (3.15) vanishes as the integrand is bounded. Since  $Y_x = 0$  at  $x = \pm W$  from (3.14) the first term in the first line of (3.15) also vanishes. The remaining terms then give, after some simplification,

$$\lim_{W \rightarrow 0} \int_{-W}^W \left\{ \frac{\Pi a}{4} \left[ (2Y + a) e^{-2Y/a} \right] Y_{xx} + Q''(x) Y e^{-Y/a} \right\} dx = 0. \quad (3.16)$$

Now define the shock width, or jump in  $Y(x)$  across  $x = 0$ , by  $\langle Y \rangle$ , so

$$\langle Y \rangle = \lim_{W \rightarrow 0} [Y(W) - Y(-W)] = Y_- - Y_s, \quad (3.17)$$

and  $\langle Q \rangle = 1$ . Taking the indefinite integral of (3.15) from  $-W$  to  $x$ , integrating the result across the outflow from  $-W$  to  $W$  as  $W \rightarrow 0$ , integrating by parts and simplifying using (3.16) gives

$$\begin{aligned} \frac{a^2 \Pi}{2} \langle Y \rangle + \frac{\Pi a^2}{4} \langle (Y + a) e^{-2Y/a} \rangle \\ + \lim_{W \rightarrow 0} \int_{-W}^W x \left\{ \frac{\Pi a}{4} \left[ (2Y + a) e^{-2Y/a} \right] Y_{xx} + Q''(x) Y e^{-Y/a} \right\} dx = 0. \end{aligned} \quad (3.18)$$

In the limit  $W \rightarrow 0$

$$Y''(x) \rightarrow \langle Y \rangle \delta'(x), \quad Q''(x) \rightarrow \delta'(x), \quad (3.19)$$

where  $\delta(x)$  is the Dirac delta function. Simplifying (3.18) then gives the required jump condition

$$\frac{a^2 \Pi}{2} \langle Y \rangle + \frac{\Pi a^2}{4} \langle (Y + a) e^{-2Y/a} \rangle - \frac{\Pi a}{4} \langle Y \rangle \left[ (2Y + a) e^{-2Y/a} \right]_{x=0} - \left[ Y e^{-Y/a} \right]_{x=0} = 0, \quad (3.20)$$

where for any  $g(Y)$ , we define  $[g(Y)]_{x=0}$  as

$$[g(Y)]_{x=0} = [g(Y_-) + g(Y_s)] / 2. \quad (3.21)$$

We have the first equation (3.20) to solve for the three unknowns ( $Y_-$ ,  $Y_s$ ,  $Y_+$ ). Next, we introduce a steady soliton in the constant  $Q = 1$  region by imposing the conditions (2.16) derived from the travelling-wave solutions of the dispersive PV equation. We require that the soliton joins to  $Y_s \neq Y_+$ , which gives the second equation

$$a^3 e^{-2Y_s/a} - 4a(a^2 - 1)e^{-Y_s/a} + \alpha_+ Y_s + E_+ = 0, \quad (3.22)$$

with the constants  $\alpha_+$ ,  $E_+$  determined from (2.16).

Since  $Y_+$ ,  $Y_-$  are linked by the hydraulic flux function  $Q_e(Y) = \Phi$ , the final equation is given by

$$\frac{a^2}{2} + (1 - a^2)e^{-Y_+/a} + \frac{a^2}{2}e^{-2Y_+/a} = \frac{a^2}{2} - a^2e^{-Y_-/a} + \frac{a^2}{2}e^{-2Y_-/a} = \Phi. \quad (3.23)$$

Solving (3.20), (3.22), (3.23) simultaneously (and requiring  $Y_+ \leq Y_s < Y_-$ ) gives the values of ( $Y_-$ ,  $Y_+$ ,  $Y_s$ ) for  $\Pi = -1$ . The shock solution is an unphysical artefact of the dispersive equation in the limit  $W \rightarrow 0$  that, however, predicts the values of  $Y_-$  and  $Y_+$  found in the numerical solutions of the full problem.

The steady hydraulic and dispersive  $W \rightarrow 0$  width predictions give the upper or lower bounds of  $Y_{\pm}$  for  $\Pi = -1$  such that

$$\begin{aligned} (Y_-)_{W=0, -1} &:= (Y_-)_{\max, -1}, & (Y_-)_{\text{hyd}, -1} &:= (Y_-)_{\min, -1} \\ (Y_+)_{W=0, -1} &:= (Y_+)_{\min, -1}, & (Y_+)_{\text{hyd}, -1} &:= (Y_+)_{\max, -1}, \end{aligned} \quad (3.24)$$

where *hyd* refers to the hydraulic predictions, giving an upper (*max*) and lower bound (*min*) to the steady current widths for some Rossby radius  $a$ . Figure 5 compares the numerical steady dispersive solutions for different  $W$ ,  $a$  values for  $\Pi = -1$  with the theoretical current widths  $Y_{\pm}$ . For small widths the upstream  $Y_-$  value is close to the theoretical  $(Y_-)_{\max}$  value. As the outflow width increases from  $W = 1$  to  $W = 100$  in the  $a = 1.3$  case, the current widths converge towards the hydraulic prediction  $(Y_-)_{\min}$ . The full QG solutions for a point source  $W = 0$  closely align with the narrow outflow case: in the  $W = 1$  dispersive simulations, a shock appears at  $Y_s$  where the soliton that matches the current widths for the full problem terminates.

### 3.3. The validity of the $W \rightarrow 0$ predictions and overturning

For all width outflows as  $t \rightarrow \infty$ , the time-dependent PV equation determines  $\Phi$  (from which all of  $Y_+$ ,  $Y_-$ ,  $\alpha_{\pm}$ ,  $E_{\pm}$  are determined) such that

- (i) There is a hydraulic constant-width current at one of the edges of the source width which stipulates  $Y_x(x = -W\Pi) = Y_{xx}(x = -W\Pi) = 0$  as  $\psi \equiv \psi^0$  here.
- (ii) The flow is critically controlled, where flow moves from subcritical flow far upstream ( $Y_-$ ) to supercritical flow far downstream ( $Y_+$ ) for  $\Pi = -1$ , and is supercritical everywhere for  $\Pi = +1$ . In the hydraulic solution, the current width is critically controlled at the edge of the source, but this condition is relaxed in the dispersive equation, being true only as  $W \rightarrow \infty$ . Dispersion means that  $\Phi$  depends on the width of the outflow.

For positive PV outflows, moving from subcritical to supercritical flow in the dispersive equation requires  $C(Y)|_{Q=0, \Pi=+1} \geq 0$ . This implies  $Y \leq 0$  upstream for the steady system for all  $W$ , and equality is only reached provided  $W = \infty$  (i.e. the hydraulic case). The wave always overturns for outflows  $W < \infty$  in the full problem as seen in § 5, but long-wave theory returns single-valued solutions that cannot capture this case. While the hydraulic solution indicates overturning by producing shocks, the dispersive solution instead allows



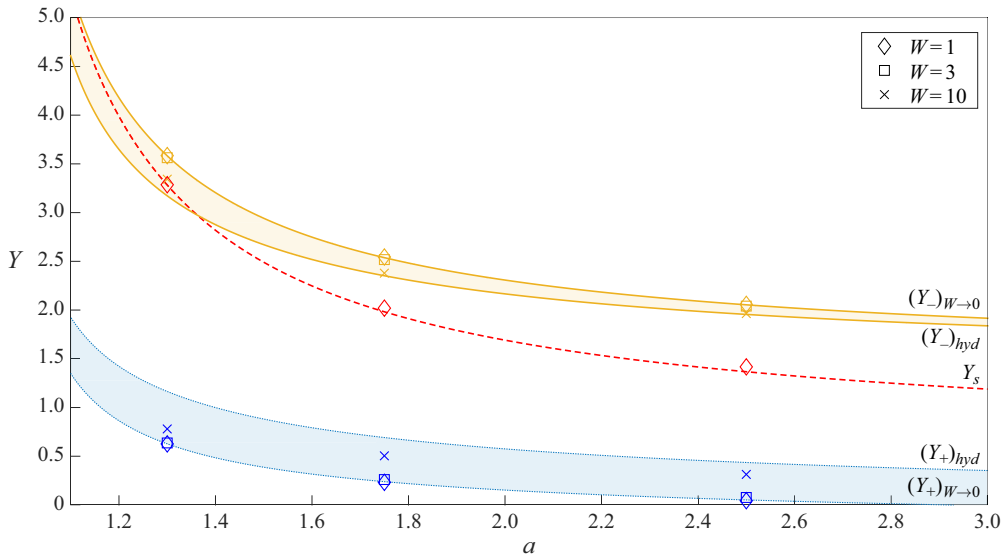


Figure 7. The predicted steady dispersive-current widths  $Y_-$ ,  $Y_+$  at different values of  $a$  for  $\Pi = -1$ . The shaded regions for both  $Y_+$  (lined edge, yellow) and  $Y_-$  (dotted edge, blue) show the range of width values based on the outflow width  $W$ . The  $Y_s$  value (red, dashed) gives the location of the shock for a point source outflow. Also plotted are numerical simulations of the steady dispersive equation at  $a = 1.3, 1.75, 2.5$  at different widths  $W = 1, 3, 10$ .

the coastal front to reach values  $Y < 0$ . Overturning decreases with increasing outflow width, and this is reflected in the dispersive equation by decreasing how far below the coast the front reaches. Hydraulic solutions alone are sufficient to determine the current widths of the full problem provided  $\Pi = +1$  with the full QG solutions indicating that  $\Phi$  is independent of  $W$ , as expected in the absence of dispersion.

In the negative PV case, the  $W \rightarrow 0$  treatment matches remarkably with the steady dispersive integrations seen in figure 7. As the outflow width decreases, the current widths tend towards the  $(Y_{\pm})_{W \rightarrow 0}$  analytically determined values as seen in the  $W = 1$  and  $W = 3$  numerical simulations. At  $W = 10$  these values align more closely with the hydraulic widths and all lie comfortably in the shaded region that represents the range of solutions for any  $W$ . In the  $W \rightarrow 0$  case, the location of the shock is well predicted by the  $W = 1$  numerical steady solution and this is where the  $Q = 1$  soliton terminates. The dependence of the outflow width on the range of values  $Y_{\pm}$  is also captured in the full problem when  $\Pi = -1$ , as discussed further in § 5. For sufficiently large Rossby radius  $a$ , the downstream current reaches the coast,  $Y_+ = 0$ . This is seen in the QG solutions but is not found in the hydraulic solution, where the downstream current always reaches the coast via a rarefaction.

## 4. The leading frontal regions

### 4.1. The time-dependent dispersive long-wave equation

With the widths  $Y_+$  and  $Y_-$  of the currents leaving the source region determined, it remains to consider the propagation of the dispersive fronts leading the currents. Table 1 summarises the notation used below. In order to numerically solve the unsteady dispersive equation (2.14) noting the three spatial derivatives in  $Q(x)$ , we require that the flux is sufficiently smooth so that at least the third derivative is bounded. For the integrations

Name	Description
$Y_+$	Constant-width current upstream from source outflow
$Y_-$	Constant-width current downstream from source outflow
$Y_I$	Width of intrusion (or half-intrusion) that connects the current width to the coast
$s_I$	Speed of the intrusion (or half-intrusion)
$Y_s$	Width of the soliton edge resulting from DSW formation
$\tilde{s}_I$	Speed of the soliton edge
$s_r$	Speed of the rarefaction at coast $Y = 0$

Table 1. The notation for the different wave structures in the PV front.

below, we use the flux function

$$Q_4(x) = \begin{cases} 0 & x \leq -W \\ \frac{8}{9} \sin^4 \left( \frac{\pi(x+W)}{3W} \right) & -W < x \leq 0 \\ 1 - \frac{8}{9} \sin^4 \left( \frac{\pi(x-W)}{3W} \right) & 0 < x < W \\ 1 & x \geq W. \end{cases} \quad (4.1)$$

Using  $Q(x) = Q_4(x)$  in (4.1) ensures that there are no discontinuities in the boundary condition (2.4). Simulations were also attempted with simpler functions, but there was very little difference in the results in either the full problem or the dispersive integrations.

A simple fourth-order Runge–Kutta scheme is used to advance the equation in time using a pseudo-spectral method, where the equation is Fourier transformed in  $x$  and solved as an ODE in Fourier space, and is then transformed back into real space. The domain is periodic and so we require the flux function to also be periodic. In practice, we truncate the domain to  $x = L$ ,  $L \gg 1$ , and to maintain periodicity, the flux function must return to 0 (its upstream value) downstream. We make this descent sufficiently gradual so as not to interfere with the evolution of the outflow. Here,  $Q_4(x)$  is reduced to 0 using a wide tanh function. We also apply de-aliasing following Orszag (1971) to remove otherwise growing high-wavenumber contributions.

#### 4.2. Compound-wave structures and dispersive-shock-wave fitting

The structure of the PV front can be seen as a composition of different wave structures discussed in JJ20. Two far-field states can be connected by a shock, rarefaction or compound shock–rarefaction depending on the specific conditions in the hydraulic PV equation (2.10). Compound-wave structures occur if  $Q_e(Y)$  is not convex in the region of interest, which means that the interval  $[Y_-, Y_+]$  contains a turning point  $Y_{turn}$  of  $Q_e(Y)$  where  $C(Y_{turn}) = Q'_e(Y_{turn}) = 0$ ; that is,  $Y_{turn} \in [Y_-, Y_+]$ .

Importantly, the governing dispersive equation also forms compound-wave structures when  $Q_e(Y)$  is not convex. Although rarefactions still occur, far-field states are instead linked by kink solitons or intrusions analogous to a shock, or by a DSW provided  $Y_+ \neq 0$ . Here, a DSW is a wave structure slowly modulated in amplitude and frequency connecting two far-field states with different propagation speeds at each edge: one being a linear wavepacket and the other a solitary wavepacket. The dispersive-shock fitting method (El 2005) that analyses DSW properties is valid if the governing PV equation satisfies a certain set of conditions outlined in Appendix A.1.

For solutions of the form  $Y = Y_\infty + \eta e^{i(kx - \omega t)}$ ,  $\eta \ll \mathcal{O}(1)$  of waves propagating on a background  $Y_\infty$ , the governing PV equation for constant  $Q(x) = Q$  has a linear dispersion relation, where  $\mathcal{O}(\eta^2)$  terms or higher are ignored, given by

$$\omega(k) = C(Y_\infty)k - \frac{a^2 \Pi}{4} \mathcal{G}(Y_\infty)k^3, \quad (4.2)$$

where  $C(Y) = (Q/a + a\Pi)e^{-Y/a} - a\Pi e^{-2Y/a}$ ,  $\mathcal{G}(Y) = a - (a + 2Y)e^{-2Y/a}$ .

We denote the linear-wave-edge wavenumber as  $k$  with dispersion relation  $\omega(k)$ , and the conjugate wavenumber of the solitary-wave edge as  $\tilde{k}$ , typically defined as the inverse half-width of the solitary wave, with conjugate dispersion relation  $\tilde{\omega}(\tilde{k}) = -i\omega(ik)$ . In this problem the far-field states are given by  $Y_I \neq 0$  (the intrusion width) and either  $Y_-$ ,  $Y_+ \neq 0$  according to the sign of the PV  $\Pi$ . We can find the wavenumber or conjugate wavenumber by solving the ODEs derived by El (2005) to obtain JJ20 for general constant  $Q(x) = Q$

$\Pi = -1$  :

$$k_-^2 = \frac{-8}{3a^2 \mathcal{G}(Y_-)^{2/3}} \int_{Y_I}^{Y_-} \frac{C'(Y)}{\mathcal{G}(Y)^{1/3}} dY, \quad \tilde{k}_I^2 = \frac{8}{3a^2 \mathcal{G}(Y_I)^{2/3}} \int_{Y_-}^{Y_I} \frac{C'(Y)}{\mathcal{G}(Y)^{1/3}} dY, \quad (4.3)$$

$\Pi = +1$  :

$$k_+^2 = \frac{8}{3a^2 \mathcal{G}(Y_+)^{2/3}} \int_{Y_I}^{Y_+} \frac{C'(Y)}{\mathcal{G}(Y)^{1/3}} dY, \quad \tilde{k}_I^2 = \frac{-8}{3a^2 \mathcal{G}(Y_I)^{2/3}} \int_{Y_+}^{Y_I} \frac{C'(Y)}{\mathcal{G}(Y)^{1/3}} dY, \quad (4.4)$$

where  $k_-$  is the wavenumber of the linear-wave edge ( $\tilde{k}_I = 0$  here), and  $\tilde{k}_I$  is the conjugate wavenumber of the solitary-wave edge ( $k_- = 0$  here).

Thus, the DSW forms a compound-wave structure with the upstream steady current ( $Y_-$ ,  $\Pi = -1$ ), where the DSW travels leftward from the linear-wave edge at  $Y_-$  to the solitary-wave edge at  $Y_I$  where it connects to an intrusion on the left; or with the downstream steady current ( $Y_+$ ,  $\Pi = +1$ ), where the DSW travels rightward from the linear-wave edge at  $Y_+$  to the solitary wave-edge at  $Y_I$  where it connects to an intrusion on the right. The propagation speeds of the solitary- and linear-wave edges are

$$s_\pm = \frac{\partial \omega}{\partial k}(Y_\pm, k_\pm), \quad \tilde{s}_I = \tilde{\omega}(Y_I, \tilde{k}_I)/\tilde{k}_I, \quad (4.5)$$

computing the speeds and the amplitude of the solitary wave at  $Y_I$ , denoted by  $Y_s$ , as well as the wavelength of the linear wave at  $Y_\pm$ . Sections 4.3 and 4.4 give examples of DSWs.

### 4.3. The structure of the PV front: the $\Pi = +1$ positive PV case

#### 4.3.1. Upstream of the source, $x < -W$ : $Q = 0$ , $\Pi = +1$

The upstream flow of  $\Pi = +1$  is well captured by the hydraulic theory of JSM17. The flow is led by a shock and terminates at the edge of the source outflow and control point  $x = -W$ , so  $Y_- \equiv 0$ ,  $x \leq -W$  for all  $a$ . The unsteady dispersive equation is ignored as it gives a poor representation of the upstream flow, predicting negative values to indicate wave overturning as discussed in § 3.1.2.

#### 4.3.2. Downstream of the source, $x > W$ : $Q = 1$ , $\Pi = +1$

Downstream the source outflow,  $x > W$ , the flux function  $Q_e(Y)$  is always non-convex in the solution if

$$Y_{turn} = a \ln \left( \frac{2a^2}{a^2 + 1} \right) \geq 0. \quad (4.6)$$

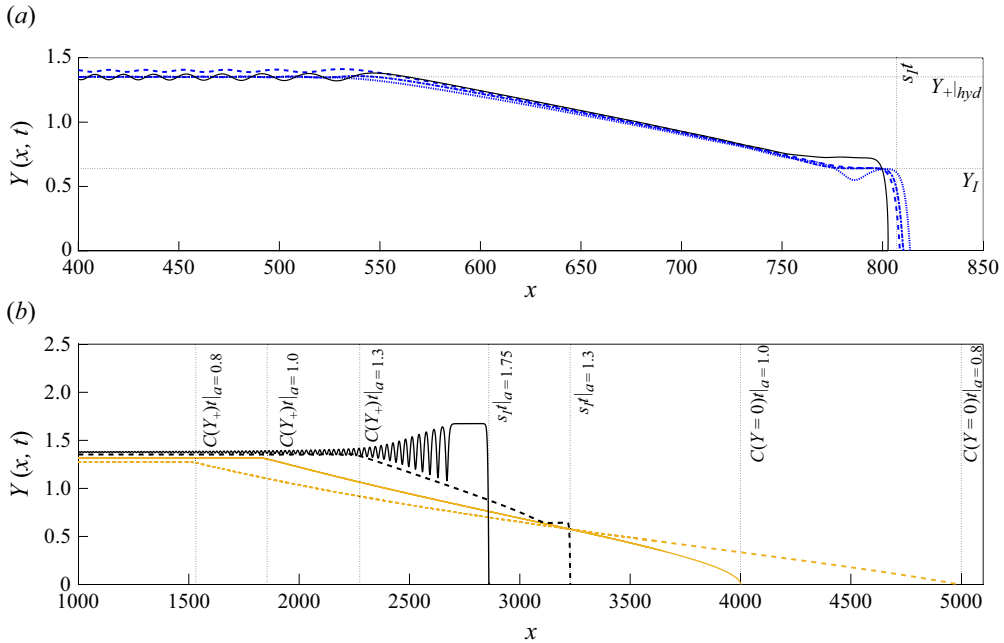


Figure 8. (a) Dispersive solution for  $\Pi = +1$ ,  $a = 1.3$  and widths  $W = 3, 10, 20$  (overlaid as blue; dashed, dash-dotted, dotted respectively), compared directly with the point source contour-dynamics simulation (black) at time  $t = 1000$ , focusing on the  $Y_+$  region and upstream. (b) Similar to top but for width  $W = 10$  and  $a = 0.8, 1.0, 1.3, 1.75$  (yellow-dashed, yellow, black-dashed, black, respectively) run until  $t = 4000$ . The dotted lines in both figures correspond to the theoretical predictions of the structure's locations.

For  $a < 1$  a rarefaction joins these states and thus we denote  $a_{r,+1} = 1$  as the value of  $a$  when a rarefaction just forms. Equation (4.6) is satisfied provided  $a \geq 1$ , where an intrusion connects the downstream current  $Y_+$  to the coast with a finite slope and current width  $Y_I$  determined by (2.18) and (2.20). A rarefaction, if it occurs, propagates according to the equation

$$\frac{x}{t} = C(Y) = \frac{1}{a} \left( 1 + a^2 \right) e^{-Y/a} - a e^{-2Y/a}, \quad C(Y_+) < C(Y) < C(Y = Y_{join}) \equiv \frac{1}{a}, \quad (4.7)$$

where  $Y_{join}$  refers to  $Y = 0$  if a rarefaction fully joins to the coast, or  $Y_I$  if a rarefaction joins to an intrusion instead.

We also require for any soliton or intrusion that the stationary points of  $Y_\xi$  in (2.15) must be local minima (representing a stable equilibrium of the far-field states), i.e.

$$v''(Y_I) > 0 \implies |s_I| > |C(Y_I)|, \quad (4.8)$$

consequently, an intrusion always overtakes a rarefaction and joins the far-field state to the coast. This forms a constant-width current region that is referred to herein as a ‘shelf’. We can calculate the values for which the shelf is wider or narrower than the immediate downstream current  $Y_+$  by determining when

$$Y_I = (Y_+)_{hyd}. \quad (4.9)$$

We denote the value of  $a$  for which (4.9) is satisfied by  $a_{I,+1}$ . Then for all  $a > a_{I,+1}$ , the intrusion shelf always remains wider than the constant-width downstream current  $Y_+$ , leading to DSW formation. A shelf cannot form if the speed of the leading soliton edge of

List of downstream behaviours according to the value of  $a$  ( $\Pi = +1$ )

Name	Description	Value (2 d.p.)
$a_{r, +1}$	Lower limit of $a$ when an intrusion forms	1.00
$a_{I, +1}$	Lower limit of $a$ when a DSW forms	1.62
$a_{crit, +1}$	Lower limit of $a$ when a constant-width shelf no longer forms	1.99

Table 2. The values of  $a$  where different behaviours of the upstream PV front form for  $\Pi = +1$ .

the DSW  $\tilde{s}_I$  matches the speed of the intrusion  $s_I$ , which occurs when

$$\tilde{s}_I = s_I. \quad (4.10)$$

We denote the value of  $a$  for which (4.10) holds by  $a_{crit, +1}$ . For  $a > a_{crit, +1}$ , a wall-bounded wavetrain joins the far-field current to the coast as illustrated in § 4.5. The values of  $a_{r, +1}$ ,  $a_{I, +1}$  and  $a_{crit, +1}$  are given in table 2.

The type of structures that form also vary with the outflow width  $W$  in the dispersive equation. However, as noted in § 3.3, this is an artefact of the dispersive equation which does not reflect the behaviour of the full problem. Although changing the source width  $W$  does not affect  $Y_+$  in the full QG equations, it introduces more waves to the system due to dispersion. Herein, irrespective of  $W$ , we only use hydraulic solutions  $(Y_+)_{hyd}$  to estimate the actual downstream current width.

Figure 8(a) shows the numerical differences in the downstream behaviour by comparing the point source  $W = 0$  contour dynamics with the dispersive dynamics at widths  $W = 3, 10, 20$  for  $a = 1.3$ . In the  $W = 3$  case, the dispersive dynamics captures the waves propagating upstream of the source, but the  $W = 10, 20$  outflows capture  $Y_+$  better and so the simulations below are restricted, unless noted, to the width  $W = 10$  for  $\Pi = +1$ . This width closely matches to the point source prediction of  $Y_+$ , yet is not so large that dispersive waves interfere with the solution (as with  $W = 20$ ). The contour dynamics also matches reasonably well to the predicted intrusion location at  $t = 500$  from travelling-wave theory. This is shown further in figure 8(b) where the predicted intrusions, rarefactions  $C(Y = 0)$  and long-wave propagation  $C(Y = Y_+)$  locations align well at  $t = 4000$  for a range of values of  $a$ .

We verify El's technique for  $a = 1.75 > a_{I, +1}$  where DSWs can form. Figure 9 shows a DSW propagating to the right downstream at  $t = 10000$  (where the DSW is fully developed), where there is a rightwards solitary-wave leading edge and a linear-wave trailing edge, terminating by an intrusion (a kink-DSW structure). As the DSW develops, the outflow sets the downstream frontal width to  $(Y_+)_{hyd}$  almost immediately (compared with DSW formation) and propagates rightwards as an almost pure wavetrain (see figure 19(b) at time  $t = 200$ ). This leading wave amplitude continues to grow until it is limited by the width of the now fully formed intrusion (see figure 19(b) at time  $t = 500$ ), determining the height and speed of the soliton edge. The soliton edge falls behind the intrusion, which travels faster to form a constant-width shelf, and thus forms the DSW. The intrusion has corresponding width and speed  $Y_I, s_I$  that is well matched with the theoretical travelling-wave theory; similarly, the theoretical dispersive-shock fitting matches well with the trailing, leading positions and the soliton width at the leading edge  $s_-t, \tilde{s}_I t, Y_s$  for  $t = 10\,000$ . We deduce the linear-wave wavelength of the DSW by calculating the distance  $2\pi/k_-$ , given by the two dotted lines along the trailing edge shown in the figure, again showing good agreement.

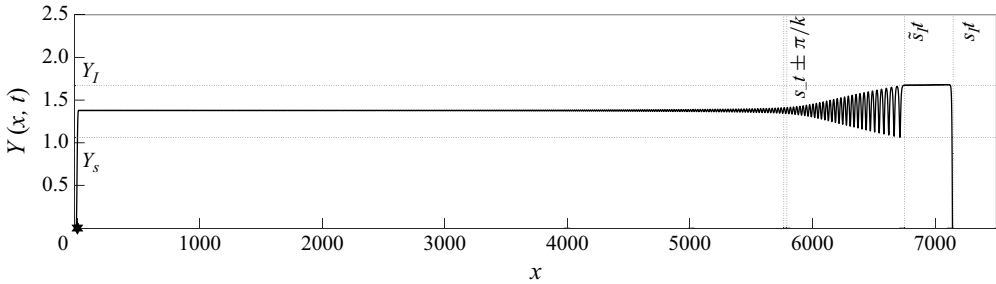


Figure 9. The numerical solution to the governing dispersive equation with  $\Pi = +1$  and  $a = 1.75$ , run until  $t = 10000$ , showing a DSW propagating upstream. The source outflow centred at  $x = 0$  is  $Q(x) \equiv Q_4(x)$  with width  $W = 10$ . The dotted lines represent the predictions of the dispersive analysis using El's technique and travelling-wave solutions.

In summary,

- (i) If  $0 \leq a \leq a_{r, +1}$ :  $Y_+$  joins the coast through a rarefaction (see [figure 8b](#), labelled yellow).
- (ii) If  $a_{r, +1} < a \leq a_{I, +1}$ : the PV front from  $Y_+$  joins the coast through an intrusion of width  $Y_I$ , and a compound-wave intrusion–rarefaction joins to the downstream current  $Y_+$ . Here,  $0 < Y_I < Y_+$  (see [figure 8b](#), labelled black-dashed).
- (iii) If  $a_{I, +1} < a \leq a_{crit, +1}$ : an intrusion joins the coast with current width  $Y_I$ , and a compound-wave intrusion–DSW joins to  $Y_+$  for all widths  $W$ . Here,  $0 < Y_+ < Y_I$  (see [figure 9](#)).
- (iv) If  $a > a_{crit, +1}$ : a shelf no longer forms, and the upstream current becomes a wall-bounded wavetrain (see [figure 15b](#)).

The parameter regimes for these cases are indicated in [figure 10](#) showing the current widths and speeds  $Y, s$  of any structures that form according to  $a$  in the  $W = 10$  dispersive integrations. In all regions  $a < a_{crit, +1}$  there is good agreement between the theoretical predictions and the numerical simulations for the speeds of the intrusions, solitons and rarefactions (panel *b*). As  $a \rightarrow 0$  the downstream speed of the rarefaction tends to infinity and numerical simulations become more challenging. If the intrusion speed  $s_I$  matches the soliton edge speed  $\tilde{s}_I$ , the soliton edge  $Y_s$  reaches the coast leading to a change in behaviour. For  $a \geq a_{crit, +1}$ , the flow forms a wall-bounded wavetrain connecting the far field to the coast. The width of the new wall-bounded wavetrain (shown in dashed lines in [figure 10](#)) differs significantly from that of the intrusion and is discussed in § 4.5.

#### 4.4. The structure of the PV front: the $\Pi = -1$ negative PV case

The structures in the negative PV case are similar to those of the positive PV case but now the current widths  $Y_{\pm}$  also depend on the source width  $W$ .

##### 4.4.1. Upstream of the source, $x < -W$ : $Q = 0$ , $\Pi = -1$

Upstream, where  $Q = 0$ ,  $x < -W$ , since  $|C(Y = 0)| < |C(Y = Y_-)| \quad \forall Y_- > 0$ , a shock forms immediately in the hydraulic equation (JSM17). In the dispersive equation, this shock is replaced by an intrusion. Unless the intrusion is of the same width as  $Y_-$ , compound-wave structures appear, independently of whether  $Q_e(Y)$  is convex or not. This is true even for  $a \leq 1$  when there are no steady solutions. Again the intrusion meets the coast with finite slope and current width  $Y_I$  predicted by (2.18) and (2.20). As in (4.8) the



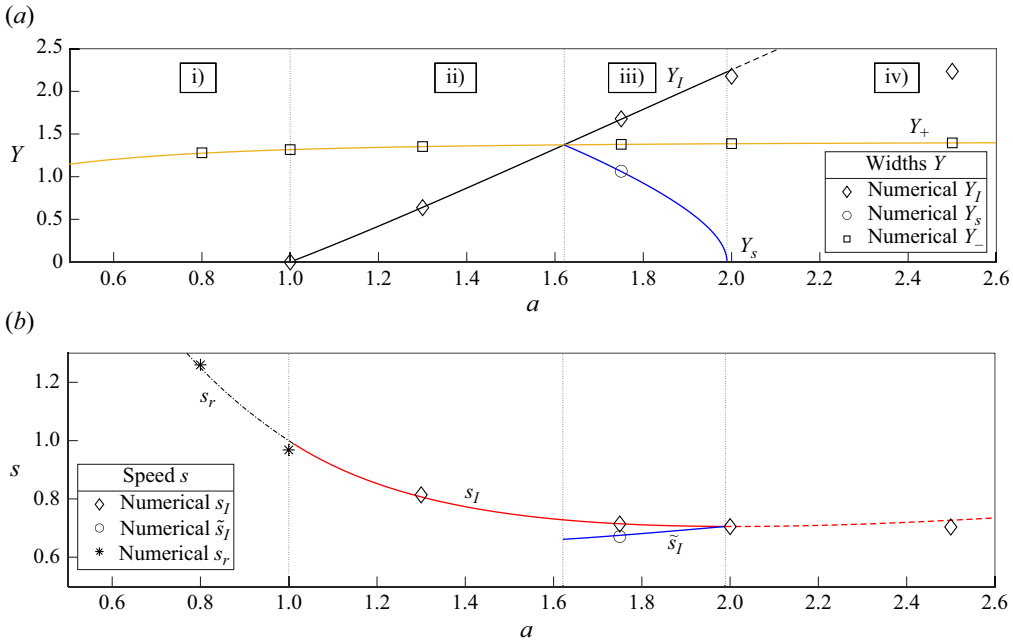


Figure 10. Downstream behaviour of the dispersive equation for  $\Pi = +1$ . The numbers i)–iv) describe regions of  $a$  where different behaviours of the front occur. (a) The theoretical and numerical ( $W = 10$ ) widths of  $Y_I$  (black, plotted diamond),  $Y_+$  (orange, plotted square) and  $Y_s$  (blue, plotted circle) if a DSW forms. (b) The respective speeds for  $s_r$  (black dash-dotted, plotted stars),  $s_I$  (red lined, plotted diamond),  $\tilde{s}_I$  (blue, plotted circle). All simulations are run for at least  $t \geq 1000$  so  $Y_+$  becomes steady.

intrusion satisfies  $v''(Y_I) > 0$ , travelling faster than any rarefaction, so the constant-width shelf formed by the intrusion lengthens over time (in the  $x$ -direction) before joining  $Y_1$  through either a rarefaction, with equation

$$\frac{x}{t} = C(Y) = ae^{-2Y/a} - ae^{-Y/a}, \quad (4.11)$$

if  $Y_I < Y_1$ , or through a DSW if  $Y_I > Y_1$ . As in § 4.3.2, we can determine the values of  $a$  for which the shelf is as wide as the constant-width current  $Y_-$  for long times by determining when

$$Y_I = Y_-, \quad (4.12)$$

and again (4.10) determines when a shelf no longer forms. Since changing the source width leads to two different bounds of  $Y_-$ , this also gives two different values of  $a$  for when these behaviours occur. These values and their corresponding notation are given in table 3. Figure 11 shows a kink-rarefaction structure for  $a = 1.3$  and an example of shelf formation in figure 11(a). The position, width and gradient of the intrusion are well predicted as is the position of the rarefaction by long-wave speed  $C(Y)$ . Figure 12 gives another example of an (upstream) DSW where its solitary edge propagates leftward. The discussion of the theoretical predictions (dotted in figure) is identical to that following figure 9 in the positive PV case, with both the predicted locations and widths agreeing well with the dispersive integrations.

List of upstream behaviours according to the value of $a$ ( $\Pi = -1$ )		
Name	Description	Value (2 d.p.)
$a_{lower, -1}$	Lower limit of $a$ when a DSW forms ( $W \rightarrow \infty$ )	1.46
$a_{higher, -1}$	Lower limit of $a$ when a DSW forms ( $W \rightarrow 0$ )	1.53
$a_{crit, -1, min}$	Lower limit of $a$ when a constant-width shelf no longer forms ( $W \rightarrow \infty$ )	1.94
$a_{crit, -1, max}$	Lower limit of $a$ when a constant-width shelf no longer forms ( $W \rightarrow 0$ )	2.02

Table 3. The values of  $a$  for the different upstream behaviours of the PV front for  $\Pi = -1$ .

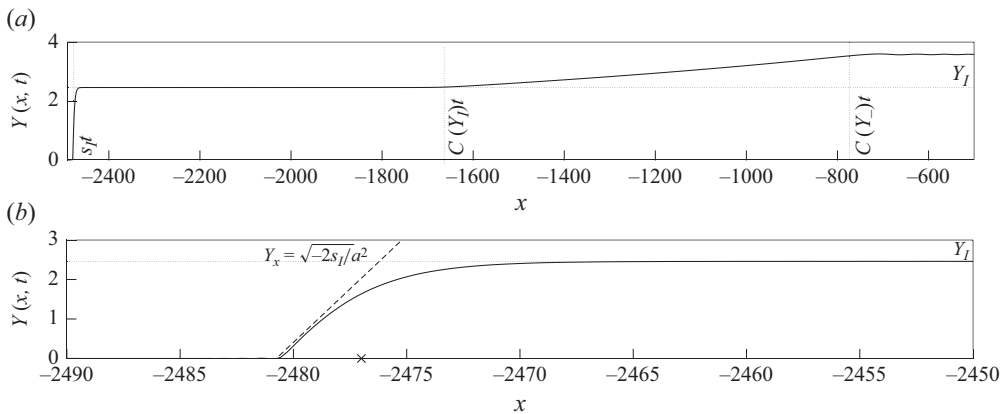


Figure 11. (a) The upstream analytical predictions (in dash-dotted) of the rarefaction and intrusion locations and the numerical integrations of the  $\Pi = -1$ ,  $a = 1.3$  dispersive equation at  $t = 10000$ ,  $W = 3$ . (b) The analytical prediction of the gradient of the intrusion, zoomed in from the top figure. Note the gradient line (dashed) is adjusted very slightly from  $s_I t$ , the predicted intrusion location (marked as a cross  $\times$ ), for clarity of comparison.

In summary,

- If  $0 \leq a \leq a_{lower, -1}$ : the PV front joins the coast through an intrusion with current width  $Y_I$ , followed by a rarefaction that joins to the downstream current  $Y_-$ . Here,  $0 < Y_I < Y_-$  (see figure 11(a)).
- If  $a_{lower, -1} < a < a_{higher, -1}$ : as in case (i) above for sufficiently large  $W$ , but through a rarefaction–intrusion for sufficiently small  $W$ .
- If  $a_{higher, -1} \leq a \leq a_{crit, -1, min}$ : for all  $W$ , an intrusion of width  $Y_I$  joins the coast followed by a DSW that joins the downstream current of width  $Y_-$ . Here,  $0 < Y_- < Y_I$  (see figure 12).
- If  $a_{crit, -1, min} < a \leq a_{crit, -1, max}$ : this gives the lower (when  $W = \infty$ ) and upper bound (when  $W = 0$ ) of when a shelf can form.
- If  $a > a_{crit, -1, max}$ : for all  $W$ , a shelf no longer forms. Instead, the downstream current terminates towards the coast via a series of modulated, periodic travelling waves, described here as a wall-bounded wavetrain (see figure 15(b)).

As in the case  $\Pi = +1$ , changing the width of the outflow produces additional waves forming a range of different phenomena that are not straightforward to quantify. For example, figure 12(b) is identical to 12(a) but a large width outflow  $W = 100$  is used instead. Using a very large outflow generates waves arising from dispersion that interact

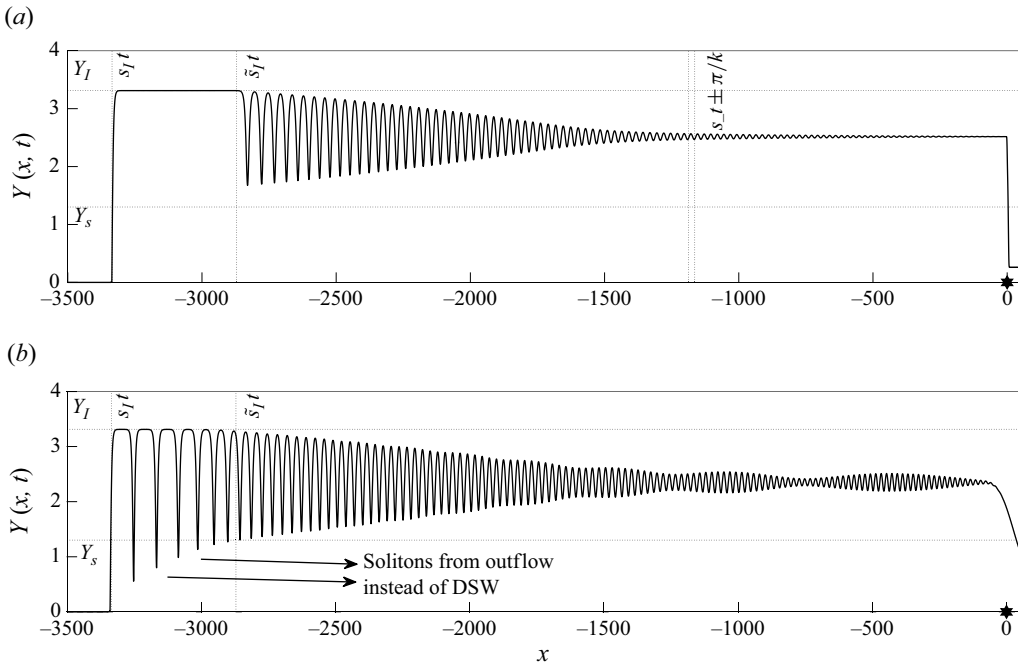


Figure 12. (a) As in figure 9 but with  $\Pi = -1$ ,  $a = 1.75$  and  $W = 3$ , run until  $t = 10000$ . (b) As in (a) but with a source outflow  $W = 100$  run until  $t = 10000$ . We observe oscillating ‘breathers’ forming upstream inside the DSW.

with the DSW forming breathers, unsteady nonlinear solutions with internal oscillations, as in Chabchoub *et al.* (2019). Hoefer *et al.* (2023) analyse an exact solution that generates breathers in the Korteweg–de Vries (KdV) equation. Further KdV analytical work has determined whether solitons can tunnel through or stay trapped in some form of mean-flow (e.g. a DSW) wave (van der Sande *et al.* 2021). In this example, the waves generated by the outflow interact with the DSW producing breathers where outflow solitons tunnel through the DSW towards the shelf. These become solitons that remain along the shelf, distinct from the solitons formed by the DSW.

Figure 13 shows the corresponding predictions (i) to (v) describing the structural behaviours as functions of  $a$  against the dispersive integrations. The shaded regions give the ranges of  $Y_s$ ,  $Y_-$ ,  $\tilde{s}_I$  depending on the value of  $W$ . There is generally good agreement with the theory for i) to iv) for small and large widths (set to  $W = 3$  and  $W = 100$ ) until  $a = a_{crit, -1, min}$  or  $a = a_{crit, -1, max}$  depending on the width of the source. The intrusion appears to reach a maximum width here before decreasing, out of line with the predictions (shown as an increasing dashed line in panel a). In figure 13(b), this corresponds to the DSW soliton edge speed  $\tilde{s}_I$  matching the intrusion speed  $s_I$  and a wall-bounded wavetrain forming as described in § 4.5.

#### 4.4.2. Downstream of the source, $x > W$ : $Q = 1$ , $\Pi = -1$

The turning point width of  $C(Y)$  is always greater than the maximum value of  $Y_+$ , given by  $(Y_+)_{max}$ , i.e.

$$Y_{turn} = a \ln \left( \frac{2a^2}{a^2 - 1} \right) > (Y_+)_{max} = a \ln \left( \frac{a^2}{a^2 - 1} \right), \quad (4.13)$$

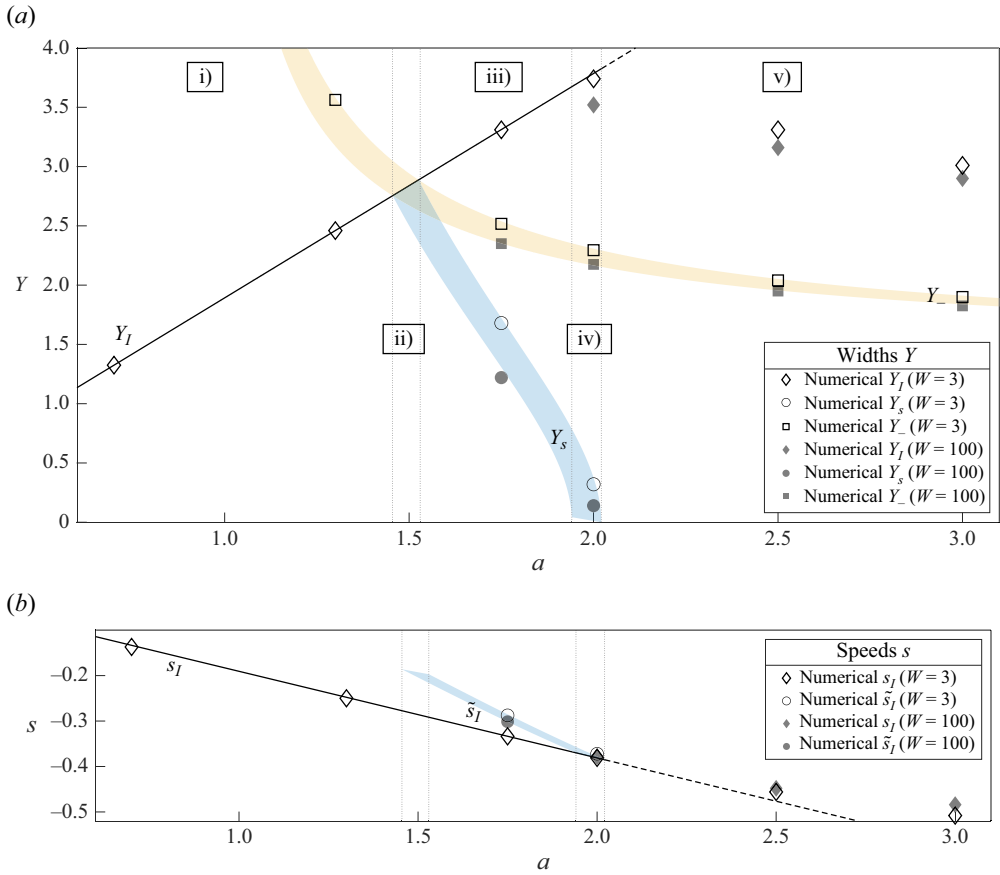


Figure 13. Upstream behaviour of the dispersive equation for  $\Pi = -1$ . The numbers i) to v) describe the regions of  $a$  where different behaviours of the front occur. (a) The theoretical and numerical widths of  $Y_I$  (plotted diamond),  $Y_-$  (shaded yellow depending on  $W$ ), and  $Y_s$  if a DSW forms (shaded blue depending on  $W$ ). (b) The theoretical and numerical speeds of  $s_I$  (plotted diamond) and  $\tilde{s}_I$  (shaded blue depending on  $W$ ). All simulations are run for at least  $t \geq 1000$  so  $Y_-$  becomes steady.

for all  $a$  and so any  $Y_+ > 0$  can be joined to the coast by a smooth rarefaction given by

$$\frac{x}{t} = C(Y) = ae^{-2Y/a} + \left(\frac{1}{a} - a\right)e^{-Y/a}, \quad C(Y_+) < C(Y) < C(Y=0) \equiv \frac{1}{a}. \quad (4.14)$$

The curvature of  $Y$  is negligible in the rarefactions and therefore so too are dispersive effects and these downstream solutions are captured well by the hydraulic equation once the dispersively determined current width is known. In the hydraulic solution  $(Y_+)_{hyd}$  is fixed for all widths, and the rarefaction always begins at the control point  $x = W$ . Figure 14 gives an example (blue circle-marked line) of a rarefaction beginning from  $x = 0$  corresponding to the fluid being released from the point source  $W = 0$ . In the dispersive solution  $Y_+$  is no longer fixed at the control point: for  $W = 0$  it is determined by solving (3.20), (3.22), (3.23) giving a constant-width current whose leading edge propagates at its long-wave hydraulic speed  $C(Y_+)$ , before joining the coast through a rarefaction. This is shown in figure 14 for  $a = 1.3$  at  $t = 10\,000$  with the downstream values of  $Y_+$  dependent on the width of the outflow. The locations of the rarefactions, shown by dotted lines in the figure, are well predicted analytically using the predicted steady widths  $Y_+$  (with  $Y_+|_{hyd}$

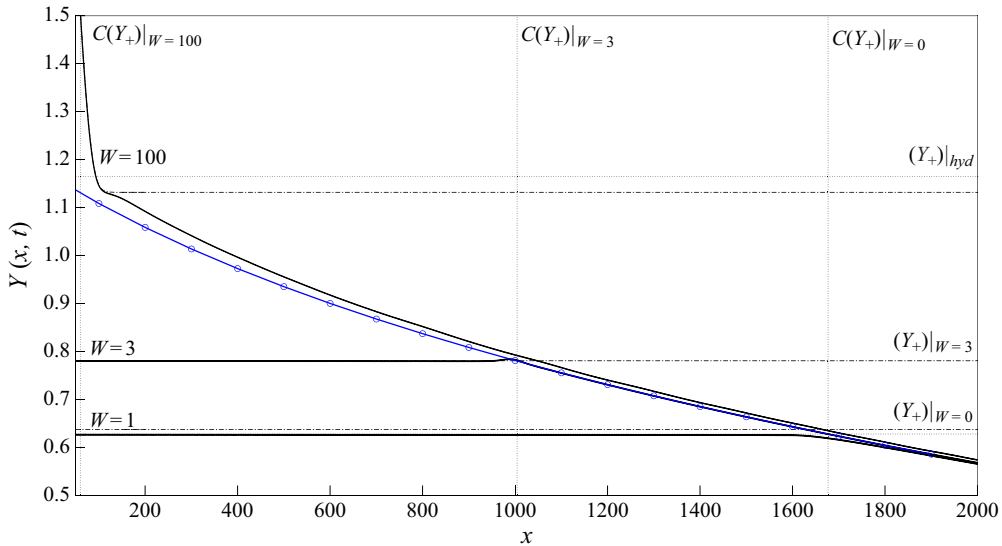


Figure 14. Dispersive integrations of downstream rarefactions for  $\Pi = -1$ ,  $a = 1.3$  at  $t = 10000$ , for widths  $W = 1, 3, 100$  (in black, labelled bottom, middle and top, respectively). The blue, circle-marked line gives the  $W = 0$  hydraulic rarefaction (4.14). For each  $W$  the predicted value of  $Y_+$  is shown dotted and the numerically determined solutions is dot-dashed. The predicted locations (vertical, dotted) on the leading edge of the hydraulic rarefactions are the long-wave speeds for each current width  $Y_+$ .

given by (3.12). When  $W = 100$  the solution has yet to fully settle, and the constant-width current is just emerging. The dispersive rarefaction can thus be viewed as a hydraulic rarefaction truncated at width  $Y = Y_+ \leq (Y_+)_{hyd}$ .

#### 4.5. The appearance of wall-bounded wavetrains

At a larger  $a$  ( $a > a_{crit, +1}$  for  $\Pi = +1$  or  $a > a_{crit, -1, max}$  for  $\Pi = -1$ ), the solitary wave leading the DSW becomes wall bounded (or coast-bounded), and propagates faster. The intrusion is replaced by a wavetrain of these faster, wall-bounded solitary waves, and the DSW truncates to the width of the wavetrain, forming a partial DSW. Hoefer *et al.* (2008) deduce the widths of wall-bounded wavetrains for the nonlinear Schrödinger piston problem using Riemann invariants. Congy *et al.* (2021) categorise this as part of a ‘DSW implosion’ with multiple behaviours, including the formation of a partial DSW, in the Benjamin–Bona–Mahony equation. They note that a quantitative description of partial DSWs requires significant knowledge of the underlying modulated wave. This knowledge is lacking for the governing dispersive PV equation (2.13) and so it does not appear possible to determine analytically the width of the wall-bounded wavetrain in the outflow problem.

From (2.15), a wall-bounded solitary wave of amplitude  $Y_I^*$  satisfies

$$v(Y=0) = v'(Y=0) = 0, \quad v(Y=Y_I^*) = 0, \quad (4.15)$$

and propagates with speed

$$s_I^* = \frac{4a(a^2 + Q\Pi)e^{-Y_I^*/a} - a^3e^{-2Y_I^*/a} + (2a^2 + 4Q\Pi)Y_I^* - (3a^3 + 4aQ\Pi)}{2\Pi Y_I^{*2}}. \quad (4.16)$$

Without the complete solution for the partial DSW, one of  $Y_I^*$  and  $s_I^*$  must be determined numerically. Figure 15 shows examples of partial DSWs propagating upstream and

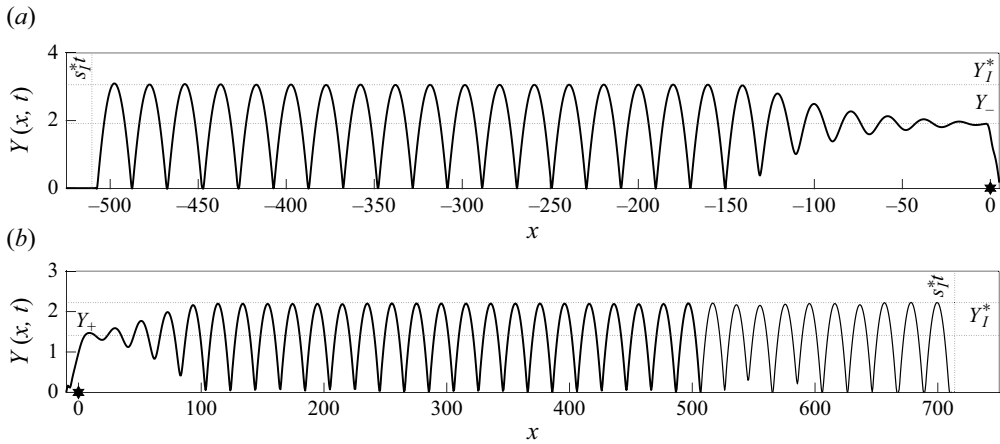


Figure 15. Wall-bounded wavetrains for  $W=3$  source outflows where (a)  $a=3.0$  and  $\Pi=-1$  and (b)  $a=6.0$  and  $\Pi=+1$  at time  $t=1000$ . Section 4.5 discusses predicting the wavetrain widths,  $Y_I^*$ , and speeds  $s_I^*$ .

downstream, where the shelf formed by the intrusion at smaller  $a$  has been replaced by a wall-bounded wavetrain. The width of the wavetrain for  $a=3.0$ ,  $\Pi=-1$  is smaller than the intrusion for  $a=1.75$  in figure 12, departing from the property of solutions of (2.18), (2.19) that the intrusion width increases with  $a$ . Using the observed, numerically determined value of  $Y_I^*$  accurately predicts the wavetrain speed  $s_I^*$ . The emergence of the wavetrain suggests that in this parameter regime solutions of the full QG equations could break into a train of eddies as appears to be happening in figure 20 below.

For larger values of  $a$ , the interface becomes more rigid, the interface deformation term  $\psi/a^2$  in (2.3) becomes negligible and the governing equation reduces to Poisson's equation. The dispersive PV equation governing the coastal front then includes a non-local Hilbert operator, significantly altering the flow dynamics (Clarke & Johnson 1997). Johnson & McDonald (2006) find exact steady solutions in the limit  $a \rightarrow \infty$  that align with the full QG solutions, suggesting that the present asymptotic expansion requires modification at sufficiently large  $a$ .

## 5. The full problem

With the structure of solutions to the dispersive equation considered we can now compare the long-wave evolution solutions with CD evolutions. The full QG system (2.3), (2.4), (2.5), (2.6) is numerically solved to a high level of accuracy using contour dynamics, incorporating contour surgery following Dritschel (1988). Solving (2.3) involves the Green's function using the modified Bessel function  $K_0(r/a)$ ,  $r = \sqrt{x^2 + y^2}$  following JJ20, which is further modified by introducing a source outflow along the wall. The velocity profiles associated with the  $Q(x) = Q_4(x)$  source outflow are computed in Appendix A.2 while the velocity profile of the point source is given in Southwick *et al.* (2017).

Figure 16 shows for  $a=1.3$ ,  $\Pi=-1$  the improvement of the present dispersive solution over the hydraulic solution in JSM17. In JSM17, hydraulic rarefactions downstream from the outflow matched closely with the contour dynamics, and this is also captured by the dispersive integrations. There is significantly greater agreement with the current widths,  $Y_{\pm}$ , adjacent to the outflow than with the hydraulic solutions



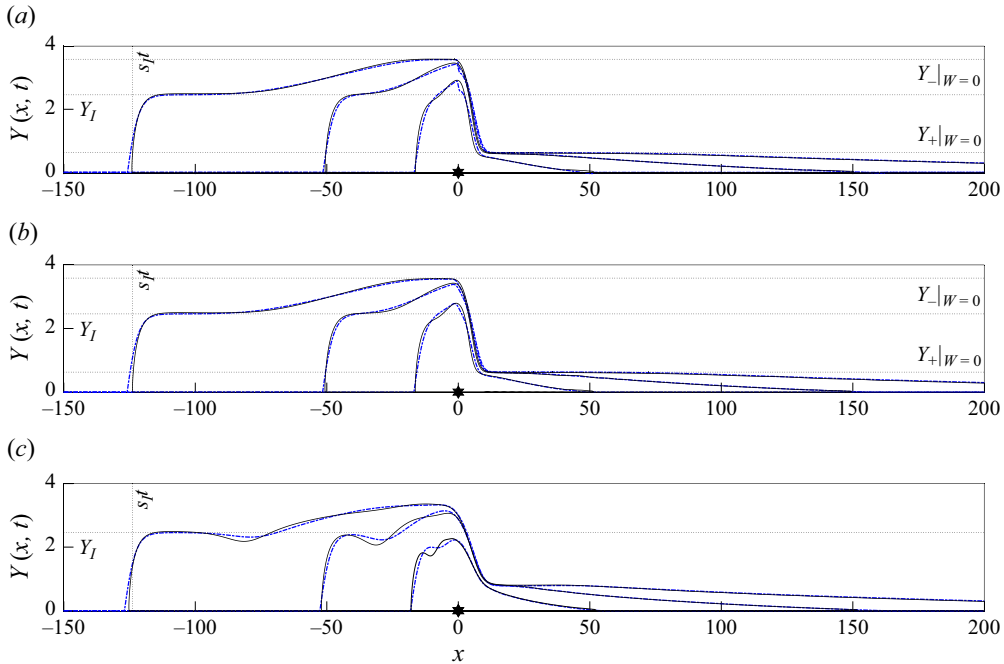


Figure 16. Numerical simulations of the contour dynamics (black) and the dispersive long-wave integrations (blue, dash-dotted) for negative PV outflows  $\Pi = -1$ , Rossby radius  $a = 1.3$  at  $t = 60, 200, 500$ , with the flux function  $Q(x) := Q_4(x)$  for different widths: (a)  $W = 1$ , (b)  $W = 3$  and (c)  $W = 10$ . In (a), (b) the theoretical dispersive long-wave  $W = 0$  values of the current widths  $Y_-|_{W=0}$ ,  $Y_+|_{W=0}$  (dotted) are overlaid for comparison, along with the theoretical intrusion widths and locations for all figures.

( $Y_{\pm}$ )<sub>hyd</sub>. Over long times  $t = 500$ , the solution converges to the steady solution where a constant-width current  $Y_-$  forms just outside the source outflow upstream  $x = -W$ , with a narrower constant-width current downstream  $Y_+$  that meets the coast through a rarefaction. This is consistent with the contour dynamics. When  $W = 1$  (figure 16a) the long-wave asymptotics produces a steep shock-like structure in the source outflow region, as predicted by § 3.2. The smaller-width sources  $W = 1, 3$  agree remarkably well with the predicted currents  $Y_-$ ,  $Y_+$  of the point source contour dynamics  $W = 0$  (omitted from the figure because it is graphically indistinguishable from the  $W = 1, 3$  simulations), agreeing with the  $W = 1$  integrations to two decimal places. Only when the width is larger ( $W = 10$ ) do the theoretical hydraulic predictions match more closely with the contour dynamics as in the steady solutions of § 3.1. The dispersive equation also accurately predicts the formation of the shelf and the location of the intrusion.

Figure 17 shows an example where the shelf is wider than  $Y_-$ , with reasonable agreement with the full problem. For larger widths ( $W = 10$ ), DSWs increasingly become out of phase with the full QG solutions, although the locations of their intrusions remain largely unchanged. This is because the initial contour that forms the front in the CD integrations is set up with an initial outflow width equal to (or slightly larger than)  $W$ , improving the numerical stability, but the dispersive solutions always propagate from  $x = 0$ . Again, the  $W = 0$  point source solutions are graphically indistinguishable from the  $W = 1, 3$  solutions.

There is also good agreement with the full problem in the  $\Pi = +1$  case, although less strongly than for the negative PV case. The full solutions always overturn near the outflow, causing the dispersive PV front to lie below the coast at negative  $Y$  values. This effect

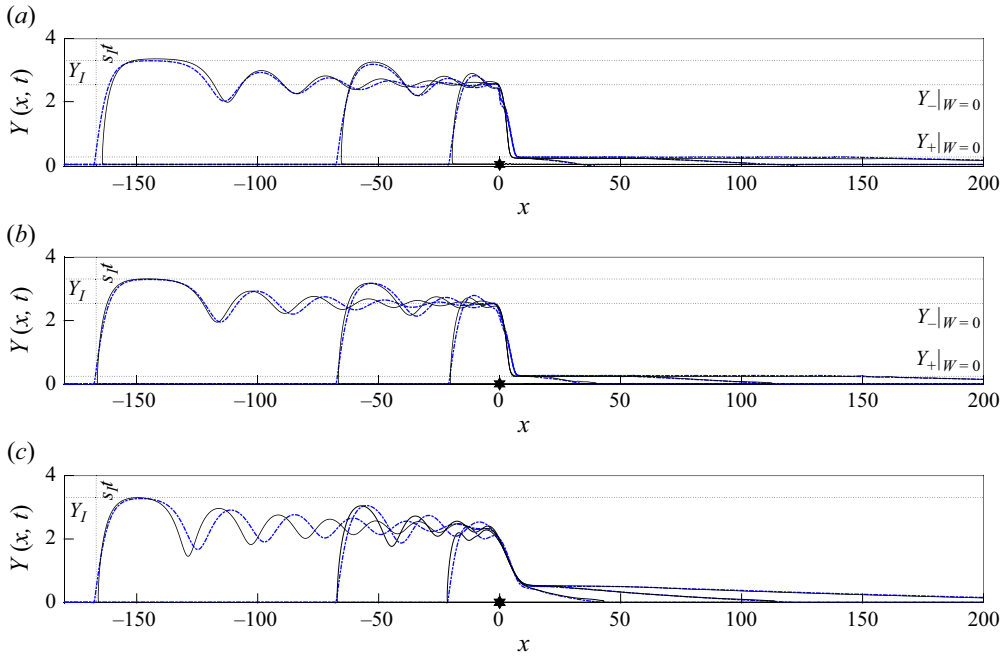


Figure 17. As in figure 16 but with Rossby radius  $a = 1.75$  at  $t = 60, 200, 500$  for: (a)  $W = 1$ , (b)  $W = 3$  and (c)  $W = 10$ . Here, the width  $Y_I$  of the intrusion is wider than the width  $Y_-$  of the flow immediately upstream outside the outflow.

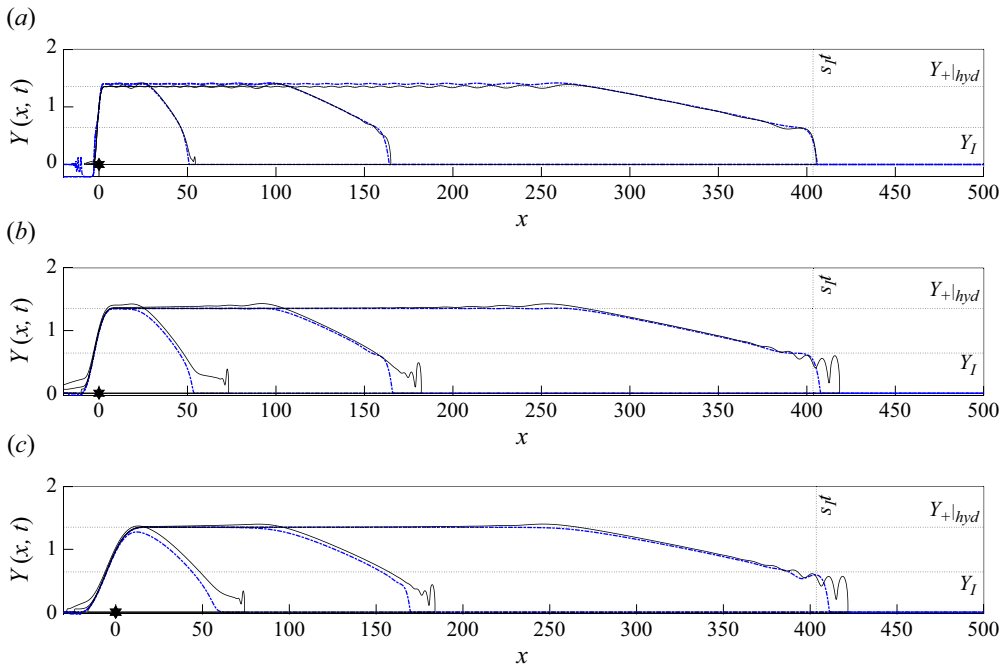


Figure 18. As in figure 16 but with  $\Pi = +1$ ,  $a = 1.3$  dispersive solutions (blue, dash-dotted) overlaid with contour dynamics (black, lined) at  $t = 60, 200, 500$  for: (a)  $W = 3$ , (b)  $W = 10$  and (c)  $W = 20$ .

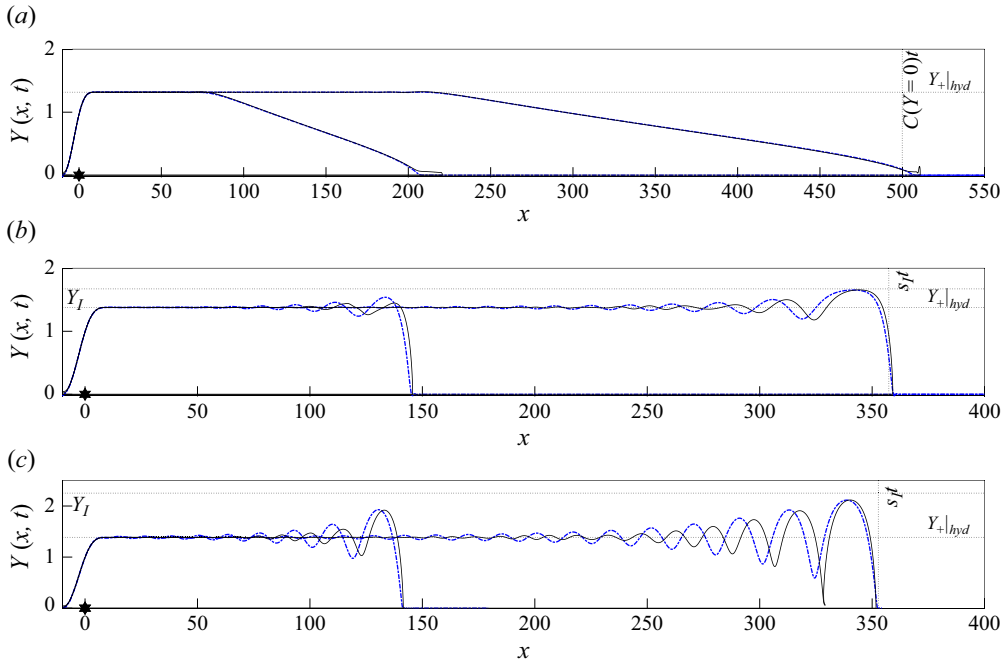


Figure 19. Dispersive integrations of the  $\Pi = +1$  regime (blue, dash-dotted) at different Rossby radii  $a = 1.0, 1.75, 2.0$  corresponding to (a), (b), (c) respectively at  $t = 200, 500$ , with source outflow width  $W = 10$  are compared with the corresponding contour dynamics (black, lined). Any theoretical predictions are given as dotted lines. The point source contour dynamics is also given as a comparison with the other solutions (black, dashed).

is most clearly seen for smaller widths in figure 18(a). The initial width of the contour is set larger than the actual source width  $W$  to prevent the overturning from breaking the contour segments in the contour dynamics, but this (initially) widens the width of the upstream current before it can settle to its true value. Simulations still generally give good quantitative downstream behaviour, especially at longer times  $t = 500$ . For all widths  $W$ , the contour dynamics chooses the current width as  $Y_+ \equiv (Y_+)_{hyd}$ .

The locations of the intrusions are better predicted for the smaller-width outflows. While the intrusion speeds remain identical for all outflow widths, increasing  $W$  alters the magnitude of overturning and increases how far the impulsively started outflow can initially propagate. The appearance of dispersive waves near the coast becomes more pronounced for the wider outflows, although there is very little dispersion (where waves are virtually constant width) immediately upstream of the source. Figure 19 compares the contour dynamics for the  $W = 10$  outflows with the dispersive integrations showing almost no difference in the case  $a = 1.0$ . In all cases, the full solution terminates through a rarefaction or intrusion corresponding to the predictions of the dispersive equation.

Beyond  $a = a_{crit, +1} \approx 1.99$ , a shelf no longer appears in the full solution; instead, a series of travelling waves that reach the coast begin to emerge. Again for larger  $a$  values the DSWs become out of phase, but the final positions of the intrusions for both  $a = 1.75, 2.0$  match well with the predicted dispersive locations  $s_I t$  at  $t = 500$  and even at the earlier time  $t = 200$ . The point source  $W = 0$  contour-dynamics simulations also agree with the  $W = 10$  dispersive integrations, the predicted leading coastal intersection and the width  $Y_+$ .

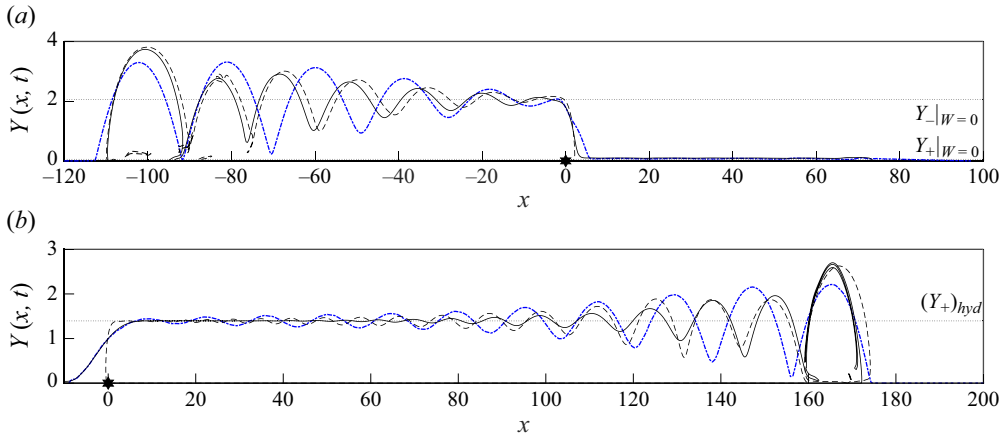


Figure 20. Dispersive integrations for the  $a = 2.5$  regime (blue, dash-dotted) with source outflow (a)  $W = 3$ ,  $\Pi = -1$ ; and (b)  $W = 10$ ,  $\Pi = +1$  compared with the corresponding contour dynamics (black, lined) at  $t = 250$ . Dotted lines give the predicted current widths. The point source contour dynamics at  $a = 2.5$  corresponding to the PV is also given as a comparison with the other solutions (black, dashed).

Figure 20, for  $a = 2.5$ , shows wall-bounded wavetrains beginning to form for  $\Pi = \pm 1$  in both the point source and finite-width source regimes. The simulations have been run for shorter times,  $t = 250$ , to mitigate eddy formation in the contour dynamics. For larger  $a$  values, the solutions align more closely with Johnson & McDonald (2006), where the positive and negative PV solutions are simply reflections about  $x = 0$  of each other. The top figure is simulated using a lower resolution, leading to a breaking of the contour near the wall, as using a higher resolution would introduce more eddies in the PV front. The dispersive-current widths  $Y_{\pm}$  capture the current widths in the full problem but the widths of the wavetrains in the dispersive integrations are an underestimate in both PV regimes. The full QG solutions form wall-bounded wavetrains but the leading structure is significantly larger than the preceding waves due to eddy formation caused by the competition of the velocities between the impulsively started outflow and its subsequent propagation. The difference in the overturning explains why the dispersive integrations and contour dynamics end downstream at different points in the  $a = 2.5$ ,  $W = 3$  simulations. While the current  $Y_+$  reaches the coast via a rarefaction in the dispersive solution, in the full problem the current overturns and strikes the coast immediately.

## 6. Discussion

JSM17 discussed the leading-order hydraulic behaviour (in the limit of large outflow width compared with current width) of coastal outflows and compared hydraulic solutions with accurate contour-dynamics simulations of the governing QG equation. Although hydraulic solutions captured much of the flow behaviour, there were significant differences in some parameter regimes. Here, we have continued the expansion to higher order, obtaining a nonlinear, dispersive, long-wave equation for the evolution of the front. At large times, the flow behaviour divides naturally into three regimes: a steady outflow region (§ 3), steady constant-width currents joined to the outflow region directly or through a truncated soliton (§ 3.1, § 3.2) and terminating unsteady propagating fronts, strongly influenced by dispersive effects (§ 4).

The widths of the steady currents are a strong function of the dispersion when the outflow PV anomaly is negative. A Rossby-wave control at the outflow, where the frontal

Rossby wave is brought to rest by the flow along the front, determines what fraction of the outflow flux moves downstream. Since the position of the control depends on the geometry of the outflow, here the outflow width  $W$ , and this means that the width of the downstream coastal current cannot be determined uniquely from global quantities like the total outflow volume flux, the PV and the density contrast. A local theory predicts the structure of the current only once the downstream flux is known. The upstream steady current width,  $Y_-$ , is largest and the downstream steady current width,  $Y_+$ , is smallest for a point source outflow. By adding dispersive terms, we identify wave overturning in the negative PV case (§ 3.3) that is absent in the hydraulic solutions.

The numerical integrations of the dispersive equation capture the full QG dynamics more accurately than the hydraulic equation, obtaining new behaviour for positive PV (§ 4.3) and accurate predictions for the downstream current widths in the case of negative PV flows (§ 3.2). A rich set of behaviours, including DSW formation and compound-wave structures (rarefaction–intrusions, DSW–intrusions) observed in the QG simulations, are discussed and quantified using standard analysis techniques for nonlinear equations (§ 4.2, El (2005), JJ20) along with a novel shock-soliton solution (§ 3.2). For sufficiently large  $a$  the dispersive equation admits travelling waves terminating in a wall-bounded wavetrain (§ 4.5) indicating a dynamical regime where coastal outflows might break into eddy trains.

For large internal Rossby radius  $a$ , the deformation term in (2.3) becomes negligible and the governing equation derived here no longer applies. Johnson & McDonald (2006) discuss this limit but do not present an analytical evolution theory so consideration of hydraulic and dispersive effects in near-rigid-interface flows remains an area for further study.

**Declaration of interests.** The authors report no conflict of interest.

## Appendix A.

### A.1. Conditions for dispersive-shock fitting

In § 4.2 we describe the method to ascertain the properties of a DSW that connects two current widths in the regions of constant flux  $Q(x) = Q$ . Here, we briefly describe, adapted from JJ20, the conditions that the governing PV equation must satisfy for this method to successfully apply:

- (i) The equation has a hydraulic (zeroth order) limit when we introduce  $X = \varepsilon x$  and  $T = \varepsilon t$  (this is done in (2.10)).
- (ii) The linear dispersion relation is real valued, given by (4.2).
- (iii) The system possesses at least two conservation laws. The first is (2.14) for  $Q(x) = Q$  constant  $Q$ . The second conservation law for constant  $Q(x) \equiv Q$ , is from JJ20 (for  $Q = 1$ ). Multiplying (2.14) by  $Y$  and simplifying gives

$$0 = \left( \frac{Y^2}{2} \right)_t + \left[ \frac{a^2 \Pi}{4} (2Y + a) e^{-2Y/a} - (Y + a)(Q + a^2 \Pi) e^{-Y/a} \right]_x \\ + \left[ \frac{-a^3 \Pi}{8} (Y_x^2 - 2Y Y_{xx}) \right. \\ \left. + \frac{a \Pi}{8} \left[ 4(Y^2 Y_x^2 + \frac{a}{2} Y Y_x^2) + a^2 (Y_x^2 - 2Y Y_{xx}) - 4a Y^2 Y_{xx} \right] e^{-2Y/a} \right]_x. \quad (\text{A.1})$$

- (iv) The equation supports periodic travelling-wave solutions parameterised by three independent variables. This is shown when writing the PV equation in potential form (2.15).

- (v) Considering slowly modulating (changing) waves means that we are able to obtain the Whitham system, which is a set of equations involving our two conservation laws (averaged over the period of a typical travelling wave) plus the wavenumber conservation equation  $\omega_x + k_t = 0$ . This system must be hyperbolic. Since the flux function  $Q_e(x, t)$  is non-convex, for certain intervals of  $Y$  the system may not be strictly hyperbolic and compound-wave structures form instead.

### A.2. The outflow velocities of the full QG equations

The streamfunction for the zero PV part of (2.3), satisfying  $\nabla^2 \psi - 1/a^2 \psi = 0$ , is found by considering the velocity of the source outflow only. Southwick *et al.* (2017) represent the associated horizontal velocity profiles  $(u, v)$  by solving the full solution in Appendix B for a general source profile as

$$\begin{pmatrix} u \\ v \end{pmatrix} = \begin{pmatrix} -\partial \psi / \partial y \\ \partial \psi / \partial x \end{pmatrix} = \frac{1}{\sqrt{2\pi}} \int_{-\infty}^{\infty} \begin{pmatrix} \kappa \\ ik \end{pmatrix} \hat{Q}(k) e^{-\kappa y} e^{ikx} dk, \quad (\text{A.2})$$

where  $\hat{Q}(k)$  is the Fourier transform of the source  $Q(x)$ , and  $\kappa = (k^2 + 1/a^2)^{1/2}$ . For the flux function  $Q_4(x)$  in (4.1), the velocity components, used in the contour dynamics to solve the full QG equation (§ 5), are given by

$$u = \frac{1}{2a} e^{-y/a} + \frac{1}{\pi} \int_0^{\infty} \frac{64 \sin(kx) \kappa e^{-\kappa y} (2 \cos(kW) + 1) \pi^4}{3(81k^5 W^4 - 180\pi^2 k^3 W^2 + 64\pi^4 k)} dk, \quad (\text{A.3})$$

$$v = \frac{1}{\pi} \int_0^{\infty} \frac{64 \cos(kx) e^{-\kappa y} (2 \cos(kW) + 1) \pi^4}{3(81k^4 W^4 - 180\pi^2 k^2 W^2 + 64\pi^4)} dk. \quad (\text{A.4})$$

The integrands in (A.3), (A.4) are bounded when  $k \rightarrow 0$  and vanish exponentially as  $k \rightarrow \infty$  for  $y > 0$ , giving rapidly converging integrals. On  $y = 0$ , the convergence of the integrals is only algebraic.

### REFERENCES

- AJANI, P.A., DAVIES, C.H., ERIKSEN, R.S. & RICHARDSON, A.J. 2020 Global warming impacts micro-phytoplankton at a long-term Pacific ocean coastal station. *Frontiers Mar. Sci.* **7**, Article 576011.
- CHABCHOUB, A., MOZUMI, K., HOFFMANN, N., BABANIN, A.V., TOFFOLI, A., STEER, J.N., VAN DEN BREMER, T.S., AKHMEDIEV, N., ONORATO, M. & WASEDA, T. 2019 Directional soliton and breather beams. **116** (20), 9759–9763. *Proc. Natl Acad. Sci. USA*
- CHANT, R.J., GLENN, S.M., HUNTER, E., KOHUT, J., CHEN, R.F., HOUGHTON, R.W., BOSCH, J. & SCHOFIELD, O. 2008 Bulge formation of a buoyant river outflow. *J. Geophys. Res.: Oceans* **113** (C1), 1–16.
- CLARKE, S.R. & JOHNSON, E.R. 1997 Topographically forced long waves on a sheared coastal current. Part 2. Finite amplitude waves. *J. Fluid Mech.* **343**, 153–168.
- CONGY, T., EL, G.A., HOEFER, M.A. & SHEARER, M. 2021 Dispersive Riemann problems for the Benjamin–Bona–Mahony equation. *Stud. Appl. Math.* **147** (3), 1089–1145.
- DRITSCHEL, D.G. 1988 Contour surgery: a topological reconnection scheme for extended integrations using contour dynamics. *J. Comput. Phys.* **77** (1), 240–266.
- EL, G.A. 2005 Resolution of a shock in hyperbolic systems modified by weak dispersion. *Chaos: Interdisciplinary J. Nonlinear Sci.* **15** (3), 3.
- GREGORIO, S., THOMAS, P., HAIDVOGEL, D., TASKINOGLU, E. & SKEEN, A. 2011 A comparison between laboratory and numerical simulations of gravity-driven coastal currents with a geostrophic theory. *Dyn. Atmos. Oceans* **56** (18), 1008.
- HOEFER, M.A., ABLOWITZ, M.J. & ENGELS, P. 2008 Piston dispersive shock wave problem. *Phys. Rev. Lett.* **100** (8), 084504.
- HOEFER, M.A., MUCALICA, A. & PELINOVSKY, D.E. 2023 KdV breathers on a cnoidal wave background. *J. Phys. A: Math. Theor.* **56** (18), 185701.



- HOLLIDAY, N., *et al.* 2020 Ocean circulation causes the largest freshening event for 120 years in Eastern Subpolar North Atlantic. *Nat. Commun.* **11** (1), 1–15.
- HORNER-DEVINE, A., FONG, D., MONISMITH, S. & MAXWORTHY, T. 2006 Laboratory experiments simulating a coastal river inflow. *J. Fluid Mech.* **555**, 203–232.
- JAMSHIDI, S. & JOHNSON, E.R. 2021 Hydraulic control of continental shelf waves. *J. Fluid Mech.* **917**, A4.
- JAMSHIDI, S. & JOHNSON, E.R. 2019 Coastal outflow currents into a buoyant layer of arbitrary depth. *J. Fluid Mech.* **858**, 656–688.
- JAMSHIDI, S. & JOHNSON, E.R. 2020 The long-wave potential-vorticity dynamics of coastal fronts. *J. Fluid Mech.* **888**, A19.
- JOHNSON, E.R. & CLARKE, S.R. 2001 Rossby wave hydraulics. *Annu. Rev. Fluid Mech.* **33** (2001), 207–230.
- JOHNSON, E.R. 2023 Bulges at vortical outflows. *Physica D: Nonlinear Phenom.* **454**, 133867.
- JOHNSON, E.R. & McDONALD, N.R. 2006 Vortical source-sink flow against a wall: the initial value problem and exact steady states. *Phys. Fluids* **18** (7), 076601.
- JOHNSON, E.R., SOUTHWICK, O.R. & McDONALD, N.R. 2017 The long-wave vorticity dynamics of rotating buoyant outflows. *J. Fluid Mech.* **822**, 418–443.
- KIDA, S. & YAMAZAKI, D. 2020 The mechanism of the freshwater outflow through the Ganges-Brahmaputra-Meghna delta. *Water Resour. Res.* **56** (6), e2019WR026412.
- KUBOKAWA, A. 1991 On the behavior of outflows with low potential vorticity from a sea strait. *Tellus A: Dyn. Meteorol. Oceanogr.* **43** (2), 168.
- LI, J., ROUGHAN, M., KERRY, C. & RAO, S. 2022 Impact of mesoscale circulation on the structure of river plumes during large rainfall events inshore of the east Australian current. *Frontiers Mar. Sci.* **9**, 1–17.
- LUO, Z., ZHU, J., WU, H. & LI, X. 2017 Dynamics of the sediment plume over the Yangtze bank in the Yellow and East China seas. *J. Geophys. Res.: Oceans* **122** (12), 10073–10090.
- MCCREARY J.P., ZHANG, S. & SHETYE, S.R. 1997 Coastal circulations driven by river outflow in a variable-density 1/2 layer model. *J. Geophys. Res.: Oceans* **102** (C7), 15535–15554.
- MENDES, R., DA SILVA, J.C.B., MAGALHAES, J.M., ST-DENIS, B., BOURGAULT, D., PINTO, J. & DIAS, J.M. 2021 On the generation of internal waves by river plumes in subcritical initial conditions. *Sci. Rep. UK* **11**, 1–12.
- MESTRES, M., SÁNCHEZ-ARCILLA, A. & SIERRA, J.P. 2007 Modeled dynamics of a small-scale river plume under different forcing conditions. *J. Coast. Res.* **2010**, 84–96.
- NAGAI, T., TANDON, A. & RUDNICK, D.L. 2006 Two-dimensional ageostrophic secondary circulation at ocean fronts due to vertical mixing and large-scale deformation. *J. Geophys. Res.: Oceans* **111** (C9), C09038, 1–18.
- ORSZAG, S.A. 1971 Elimination of aliasing in finite-difference schemes by filtering high-wavenumber components. *J. Atmos. Sci.* **28** (6), 1074–&.
- PHAM, H.T. & SARKAR, S. 2019 The role of turbulence in strong submesoscale fronts of the Bay of Bengal. *Deep Sea Res. II: Topical Stud. Oceanogr.* **168**, 104644.
- PIECUCH, C.G., BITTERMANN, K., KEMP, A.C., PONTE, R.M., LITTLE, C.M., ENGELHART, S.E. & LENTZ, S.J. 2018 River-discharge effects on United States Atlantic and Gulf coast sea-level changes. *Proc. Natl Acad. Sci. USA* **115** (30), 7729–7734.
- PRATAP, S. & MARKONIS, Y. 2022 The response of the hydrological cycle to temperature changes in recent and distant climatic history. *Prog. Earth Planet. Sci.* **9** (1), 30.
- PRATT, L.J. & STERN, M.E. 1986 Dynamics of potential vorticity fronts and eddy detachment. *J. Phys. Oceanogr.* **16** (6), 1101–1120.
- RAHMSTORF, S. 2003 Thermohaline circulation: the current climate. *Nature* **421** (6924), 699.
- VAN DER SANDE, K., EL, G.A. & HOEFER, M.A. 2021 Dynamic soliton–mean flow interaction with non-convex flux. *J. Fluid Mech.* **928**, A21.
- SOUTHWICK, O.R., JOHNSON, E.R. & McDONALD, N.R. 2017 Potential vorticity dynamics of coastal outflows. *J. Phys. Oceanogr.* **47** (5), 1021–1041.
- SUN, Y., *et al.* 2022 Spatial and temporal distribution of phytoplankton community in relation to environmental factors in the southern coastal waters of Korea. *Frontiers Mar. Sci.* **9**, 950234.
- TAO, B., TIAN, H., REN, W., YANG, J., YANG, Q., HE, R., CAI, W. & LOHRENTZ, S. 2014 Increasing Mississippi river discharge throughout the 21st century influenced by changes in climate, land use, and atmospheric CO<sub>2</sub>. *Geophys. Res. Lett.* **41** (14), 4978–4986.
- THOMAS, P.J. & LINDEN, P.F. 2007 Rotating gravity currents: small-scale and large-scale laboratory experiments and a geostrophic model. *J. Fluid Mech.* **578**, 35–65.
- WANG, T., ZHAO, S., ZHU, L., MCWILLIAMS, J., GALGANI, L., MD AMIN, R., NAKAJIMA, R., JIANG, W. & CHEN, M. 2022 Accumulation, transformation and transport of microplastics in estuarine fronts. *Nat. Rev. Earth Environ.* **3** (11), 795–805.